A PROPOSAL FOR A NEW HIGH - BANDWIDTH, E.I.T.-ENHANCED PUMP-PROBE ATOMIC MAGNETOMETER

By
Yiorgos Katsoprinakis

SUBMITTED IN PARTIAL FULFILLMENT OF THE
REQUIREMENTS FOR THE DEGREE OF
MASTER OF SCIENCE
AT
UNIVERSITY OF CRETE
VOUTES, IRAKLION
SEPTEMBER 2006

UNIVERSITY OF CRETE
DEPARTMENT OF
PHYSICS

The undersigned hereby certify that they have read and recommend to the Faculty of Graduate Studies for acceptance a thesis entitled "**A proposal for a new high - bandwidth, E.I.T.-enhanced Pump-Probe atomic magnetometer**" by **Yiorgos Katsoprinakis** in partial fulfillment of the requirements for the degree of **Master of Science**.

Dated: September 2006

Supervisor: ______________________
Iannis Kominis

Readers: ______________________
Xenofon Zotos

____
Dimitris Charalambidis

UNIVERSITY OF CRETE

Date: **September 2006**

Author: **Yiorgos Katsoprinakis**

Title: **A proposal for a new high - bandwidth, E.I.T.-enhanced Pump-Probe atomic magnetometer**

Department: **Physics**

Degree: **M.Sc.** Convocation: **September** Year: **2006**

Permission is herewith granted to University of Crete to circulate and to have copied for non-commercial purposes, at its discretion, the above title upon the request of individuals or institutions.

Signature of Author

To Mika

Table of Contents

Acknowledgements

First of all, I acknowledge the financial support from the university of Crete, FO.R.T.H. and I.K.Y. (Ι*δρυμα* Κ*ρατικων* Υ*ποτροφιων*). I would then like to acknowledge numerous helpful discussions with Dr. David Petrosyan, a true expert in quantum optics. Also, I thank all my professors in the Optoelectronics-Microelectronics master program of the University of Crete and especially professor Petros Ditsas, the guardian angel of all post-graduate students. Moreover I am grateful to have collaborated with my supervisor, Iannis Kominis, and I hope that this collaboration will continue in the future. Funny guy this one. Last, but certainly not least, I would like to thank my family and my Mika for all the support they have provided me with. One can pass with very few but few people can sustain the lack of support. Oh, and the food was great.

Iraklio, Greece
August, 2006

Yiorgos Katsoprinakis

Abstract

In recent years, atomic magnetometers have become competitive with the world standard in magnetic field measurements, the SQUIDs (Superconducting QUantum Interference Devices), rivaling their unprecedented sensitivity and finding applications in diverse fields, ranging from medicine and geology to sensitive tests of potential violations of fundamental symmetries. In this thesis we present a variation of the pump-probe magnetometer ([1], [11]), in which the magnetic field is measured via the paramagnetic Faraday rotation of the polarization plane of a linearly polarized probe laser beam passing through an optically pumped alkali vapor, subject to this magnetic field. Whereas the sensitivity of such devices is excellent at DC to low frequency AC magnetic fields, it quickly deteriorates at higher frequencies. We propose creating EIT (Electromagnetically Induced Transparency) conditions for the probe beam, which results in an increase of the useful bandwidth of the magnetometer by a factor on the order of 10^2.

Abbreviations and Symbols

TLA	**T**wo **L**evel **A**tom
TLS	**T**wo **L**evel **S**ystem
OP	**O**ptical **P**umping
P-P	**P**ump - **P**robe
RF	**R**adio **F**requency
EIT	**E**lectromagnetically **I**nduced **T**ransparency
LWI	**L**asing **W**ithout **I**nversion
RWA	**R**otating **W**ave **A**pproximation
PSD	**P**ower **S**pectral **D**ensity
spn	**S**pin **P**rojection **N**oise
psn	**P**hoton **S**hot **N**oise

Ω_p, δ_p	Probe field Rabi frequency and detuning
Ω_d, δ_d	Drive field Rabi frequency and detuning
δ_R	Raman detuning ($= \delta_p - \delta_d$)
Ω_L	Magnetic field Larmor frequency
R	optical pumping rate
R_{ex}	optical excitation rate
T_2	transverse spin relaxation time
Γ	natural decay width

Chapter 1

An Introduction to Atomic Magnetometers

1.1 Introduction

A *magnetometer* is a device used to measure the strength and, possibly, the direction of a magnetic field. In the course of history, and with K.F. Gauss pioneering the field, magnetometers have evolved from simple compass-based units to highly elaborate superconducting and quantum-based atomic apparati. In any case, among the main characteristics of a magnetometer are its *magnetic sensitivity*, which indicates the lowest measurable magnetic field, its *dynamic range*, that is the range of measurable magnetic fields, and its *bandwidth*, which is the range of AC magnetic field frequencies to which the magnetometer is sensitive. Nowadays, the field of magnetometers is dominated by SQUIDs (Superconducting QUantum Interference Devices) and atomic magnetometers, which are competing in the measurement of sub-femtoTesla fields, with SQUIDs being the industry standard.

Atomic magnetometers are of various types and they implement various detection principles: Proton precession and RF magnetometers are based on magnetic resonance techniques, EIT magnetometers - so far - measure the Zeeman shift of atomic levels via the phase shift of a probe beam passing through a coherently prepared vapor in one arm of a Mach-Zehnder interferometer and Pump-Probe magnetometers determine the magnetic field through the Faraday rotation angle of the polarization plane of a linearly polarized probe beam passing through an optically pumped vapor.

In the remainder of this Chapter we use a *toy model*, that is a simple energy level structure of a fictitious atom, to describe the operation of the pump-probe magnetometer. In Chapter 2 an introduction to Electromagnetically Induced Transparency (EIT) and Lasing Without Inversion (LWI) is given. Then, in Chapter 3 we combine the pump-probe magnetometer with EIT and propose a new type of high-bandwidth atomic magnetometer. Finally, in Chapter 4 the two types of magnetometers are studied taking into account the full level structure of ^{85}Rb and the results are compared to the toy models of the previous Chapters. Also, in the end of the same Chapter, we discuss the impact of Doppler effect on our results.

1.2 Pump-probe Magnetometer

1.2.1 Description of operation. Signal of the magnetometer

In Figure 1.1(a) we depict the setup for a pump-probe magnetometer. In order to model the way it works, we will assume that the vapor in the cell consists of simple atoms with spin-$\frac{1}{2}$ ground and excited states. In Figure 1.1(b) we can see all the interactions that take place in the cell[1]:

- In the $\hat{z}$-axis, the incoherent σ^+-polarized pump beam is pumping population from state $|\bar{g}\rangle_z = |ground_z, -\frac{1}{2}\rangle$ to $|g\rangle_z = |ground_z, \frac{1}{2}\rangle$, with an optical pumping rate R, proportional to the excitation rate R_{ex} shown in 1.1(b).
- the magnetic field rotates spins around $\hat{y}$ with a Larmor frequency $\Omega_L = \gamma B_y$, where γ is the gyromagnetic ratio, creating a spin polarization component along $\hat{\boldsymbol{x}}$ -axis, $P_x \propto B_y$

---

[1] natural decay and the magnetic field interaction look identical in both $\hat{x}$ and $\hat{z}$ axes, since the former is an isotropic procedure and in the latter, the magnetic field is along the $\hat{y}$-axis and perpendicular to the xy-plane. We thus draw these interactions only once in Figure 1.1(b)

- In the $\hat{x}$-axis, the linearly polarized probe beam is probing P_x via paramagnetic Faraday rotation of its polarization plane.

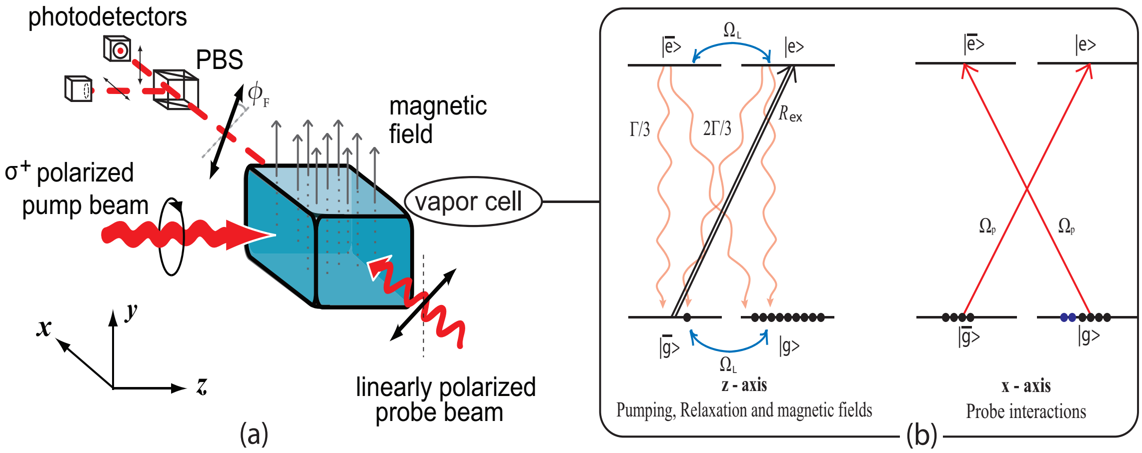

Figure 1.1: Pump-probe magnetometer model

The ground steady state population distribution is determined by the balance between the rate at which polarization is created along $\hat{z}$ ($\sim R$), the rate at which this polarization vector is rotated by the magnetic field (Ω_L) and the rate at which the spins of the atoms relax back to the thermal equilibrium distribution, $\frac{1}{T_2}$, where T_2 is the *transverse relaxation time* of the atoms discussed in Appendix A. For a very small magnetic field, $\Omega_L \ll R$, most of the population will end up in $|g\rangle_z$ creating a large polarization along $\hat{\boldsymbol{z}}$. In the absence of the magnetic field, the projection of this polarization along $\hat{\boldsymbol{x}}$ is, of course, zero, but in its presence a small $\hat{\boldsymbol{x}}$-polarization component appears due to the slight rotation of the $\hat{\boldsymbol{z}}$-polarization. So, along the propagation direction of the probe, $\hat{\boldsymbol{x}}$, the populations of states[2] $|\bar{g}\rangle$ and $|g\rangle$ will both be nearly equal to $\frac{1}{2}$, but there will be a small imbalance between them due to the magnetic field, that is:

$$\rho_{\bar{g}\bar{g}} = \frac{1}{2} - \Delta(B) \qquad \texttt{and} \qquad \rho_{gg} = \frac{1}{2} + \Delta(B) \tag{1.2.1}$$

---

[2] x index dropped: $|i\rangle_x$ states will from now on be denoted as $|i\rangle$

This small population imbalance will be linear in the magnetic field, at least for small magnetic fields which is the case of interest here, and will cause the σ^+ and σ^- components of the linearly polarized probe beam to experience slightly different indices of refraction, which, in turn, results in a rotation of the polarization plane of the probe, the *paramagnetic Faraday rotation*[3]. The Faraday rotation angle, ϕ_F, is proportional to the population difference $\rho_{gg} - \rho_{\bar{g}\bar{g}}$ and hence, it is also proportional to the magnetic field, B. If the rotated beam passes through a properly oriented[4] Polarizing Beam Splitter (PBS) and the two polarization components are measured in two photodiodes, as shown in Figure 1.1, the difference of the two photocurrents, termed the *signal of the magnetometer*, will be proportional to ϕ_F:

$$S = I_{[\updownarrow]} - I_{[\leftrightarrow]} = 2\phi_F I_{\mathtt{tr}} = 2\phi_F I_o e^{-\alpha l} \tag{1.2.2}$$

where $I_{\mathtt{tr}}$ and I_o are the photocurrents corresponding to the transmitted and incident probe intensity, respectively, α is the absorption coefficient and l the length of the cell along the propagation direction of the probe beam. Since ϕ_F is proportional to the magnetic field, the latter can be deduced from the signal of the magnetometer.

In the following we use the Bloch equations to calculate ϕ_F and then discuss the noise sources which limit the sensitivity of the pump-probe magnetometer. Finally, all quantities of interest are also studied in a density matrix approach, so as to facilitate the comparison between this type of magnetometer and its EIT-enhanced version we propose in Chapter 3 and which is also studied in the same context.

1.2.2 Bloch equations approach

- **calculation of polarizations**

Let $\mathbf{P} = P_x\hat{\boldsymbol{x}} + P_y\hat{\boldsymbol{y}} + P_z\hat{\boldsymbol{z}}$ be the ensemble average of the atomic vapor spin-polarization. In the presence of optical pumping and an applied magnetic field, the

---

[3] A more adequate explanation of the phenomenon is presented in §1.2.5

[4] by "properly oriented" we mean that, in the absence of the magnetic field, the two polarization components coming out of the PBS should carry the same power

evolution of the polarization is described by:

$$\frac{d\mathbf{P}}{dt} = \gamma\mathbf{B} \times \mathbf{P} + R\hat{\boldsymbol{z}} - \left(R + R_{\texttt{probe}} + \frac{1}{T_2}\right)\mathbf{P} \tag{1.2.3}$$

where $\frac{1}{T_2}$ is the transverse spin relaxation rate, which is assumed to be the same for all polarization components [5], $R \simeq R_{\texttt{ex}}/2$ is the pumping rate from $|\bar{g}\rangle$ to $|g\rangle$, with $R_{\texttt{ex}}$ being the excitation rate from $|\bar{g}\rangle$ to $|e\rangle$, and we have also included the probe beam pumping rate, $R_{\texttt{probe}}$, which contributes to the relaxation of spins. Assuming a DC magnetic field and setting $\gamma\mathbf{B} = \Omega_L\hat{\boldsymbol{y}}$ and expanding (1.2.3) we get:

$$\begin{aligned}
\frac{dP_x}{dt} &= -\left(R + R_{\texttt{probe}} + \frac{1}{T_2}\right)P_x + \Omega_L P_z \\
\frac{dP_y}{dt} &= -\left(R + R_{\texttt{probe}} + \frac{1}{T_2}\right)P_y \\
\frac{dP_z}{dt} &= R - \left(R + R_{\texttt{probe}} + \frac{1}{T_2}\right)P_z - \Omega_L P_x
\end{aligned} \tag{1.2.4}$$

Solving equations (1.2.4) for the steady state we get:

$$\begin{aligned}
P_x &= \frac{\Omega_L R}{{\Omega_L}^2 + \omega_c^2} \\
P_y &= 0 \\
P_z &= \frac{\omega_c R}{{\Omega_L}^2 + \omega_c^2}
\end{aligned} \tag{1.2.5}$$

The quantity

$$\omega_c = R + R_{\texttt{probe}} + \frac{1}{T_2} \tag{1.2.6}$$

is called the *bandwidth* of the magnetometer, and defines the range of AC magnetic field frequencies over which the magnetometer is sensitive. Indeed, assume an AC magnetic field with a time dependence of the form $B(t) = B_y e^{i\omega t}$, which naturally leads to the same time dependence for the $\hat{\boldsymbol{x}}$ and $\hat{\boldsymbol{z}}$-axis polarization, $P_x(t) = P_x^{(o)}e^{i\omega t}$

---

[5] the spin relaxation term along the quantization axis is the longitudinal $\frac{1}{T_1}$, but here $\frac{1}{T_2} \simeq \frac{1}{T_1}$.

and $P_z = P_z^{(o)} + P_z^{(1)} e^{i\omega t}$. Assume also that $\Omega_L = \gamma B_y \ll \omega_c$, so that the polarization along $\hat{\boldsymbol{z}}$-axis is practically unaffected by the magnetic field and equal to $P_z \simeq P_z^{(o)} \simeq R/\omega_c$. Then the first of equations (1.2.4) will be modified to:

$$i\omega \frac{dP_x^{(o)}}{dt} = -\omega_c P_x^{(o)} + \Omega_L P_z$$

and thus:

$$P_x^{(o)} = \frac{P_z \Omega_L}{i\omega + \omega_c}$$

the absolute value of which gives the $\hat{\boldsymbol{x}}$-axis polarization:

$$P_x = \frac{P_z \Omega_L}{\sqrt{\omega_c^2 + \omega^2}} = \frac{R\ \Omega_L}{\omega_c \sqrt{\omega_c^2 + \omega^2}} \tag{1.2.7}$$

The equations above clarify the reason for which ω_c is called the bandwidth of the magnetometer, since for $\omega \gg \omega_c$, $P_x \to 0$ and no polarization rotation measurement can be made on the probe beam. In terms of physical understanding, the discussion above states that the spins will not be able to follow variations of the magnetic field that happen faster than the rate at which polarization builds up.

- **calculation of Faraday rotation angle**

If we define $J_x = \sum_{i=1}^{N} J_x^{(i)}$ as the $\hat{\boldsymbol{x}}$-component of the total spin of the N-atom ensemble, we can write $\langle J_x \rangle = N P_x$. We also define the Faraday rotation angle operator, $\hat{\phi}_F$, the expectation value of which is the measured rotation angle. This operator will be proportional to J_x,

$$\phi_F = \langle \hat{\phi}_F \rangle = \kappa \langle J_x \rangle = \kappa N P_x \tag{1.2.8}$$

where the proportionality factor, κ, is expressed in various ways depending on the system. In our TLA model, far from resonance, $\kappa = \frac{\sigma}{A}\frac{\delta}{\Gamma}$, where σ is the absorption cross section, A the beam area, Γ the linewidth of the transition and $\delta \gg \Gamma$ the detuning. More rigorous expressions can be derived from equations (1.2.35) through (1.2.40) for the TLA model and, in a more complicated way, from (1.2.36) in conjunction with (3.2.3) and (3.2.7) for the EIT model.

• Signal of the magnetometer revisited

To get a feel of this result, we revisit equation (1.2.2) for the signal of the magnetometer and we see that, for our TLA model, it can be put in the form:

$$S = 2\frac{\sigma}{A}\frac{\delta}{\Gamma}NP_xI_oe^{-n_d\sigma l} \tag{1.2.9}$$

where n_d is the number density of the atoms in the cell. Also, the absorption cross section is:

$$\sigma = \frac{\Gamma}{2\pi}\frac{r_ecf}{\delta^2+(\Gamma/2)^2} \tag{1.2.10}$$

where $r_e = 2.8 \times 10^{-15}$ m is the, so called, *classical electron radius* , c the speed of light and f the oscillator strength of the probed transition.

In general, such a magnetometer is operated away from resonance, where $\phi_F \propto 1/\delta$ and $\sigma \propto 1/\delta^2$. Thus, working not very far from resonance results in substantial rotation angles, but small transmitted power due to increased absorption coming from the large value of σ in the exponent. Reversely, working very far from resonance increases the transmitted power but decreases the angle. The maximum signal is obtained for some optimum detuning from resonance which lies somewhere in between of the two extremes. In particular, for a detuning quite larger than Γ, the signal of the magnetometer is of the form:

$$S \propto \frac{\delta}{\delta^2+(\Gamma/2)^2}\ \exp\left[-\frac{\Delta^2}{\delta^2+(\Gamma/2)^2}\right] \simeq \frac{1}{\delta}\ e^{-\Delta^2/\delta^2} \tag{1.2.11}$$

and is maximized for an optimum detuning, $\delta_{\texttt{opt}}$:

$$\delta_{\texttt{opt}} = \pm\sqrt{\Delta^2+\sqrt{\Delta^4+(\Gamma/2)^4}} \simeq \pm\sqrt{2}\ \Delta \tag{1.2.12}$$

where $\Delta = \sqrt{\frac{\Gamma}{2\pi} n_d r_e c f l}$. In the following sections we will see that Δ can be expressed in a different way in the density matrix approach. A typical plot of the pump-probe magnetometer signal versus detuning is shown in Fig.4.5(a).

1.2.3 Sensitivity: a general discussion

The *sensitivity* of a magnetometer is defined as the minimum detectable magnetic field. As in any measuring device, the lower limit of the sensitivity is determined by the various noise sources in the system and the magnetic sensitivity studied here is but the noise expressed in magnetic field units. In atomic magnetometers, noise can be inherent, due to fundamental sources, or external, due to technical sources. We will introduce the two types of noise separately.

- **Fundamental noise**

We begin with the derivative of P_x with respect to B_y, computed at a frequency $\omega \ll \omega_c$, which is:

$$\left.\frac{\partial P_x}{\partial B_y}\right|_{B_y=0} = \frac{\gamma R}{\omega_c^2} = \frac{\gamma P_z}{\omega_c} \tag{1.2.13}$$

The uncertainty in the measured magnetic field is

$$\Delta B_y = \frac{\Delta\phi}{|\partial\langle\phi\rangle/\partial B_y|} \tag{1.2.14}$$

where $\Delta\phi \equiv \sqrt{\langle\phi^2\rangle - \langle\phi\rangle^2}$ is the uncertainty in the rotation angle measurement. In order to maximize the magnetic sensitivity and the measured signal the derivative $\partial\langle\phi\rangle/\partial B_y$ and P_x have to be maximum. It follows that both conditions are met when $R \approx R_{\texttt{probe}} \approx 1/T_2$. The idea is this: both the conditions above lead directly, through equations (1.2.13), (1.2.8) and (1.2.27), to the conclusion that the pumping rate R should equal the sum of $R_{\texttt{probe}}$ and $\frac{1}{T_2}$, $R = R_{\texttt{probe}} + \frac{1}{T_2}$. Now the measured signal is proportional to the probe power times the rotation angle, and since the pumping rate of the probe is also proportional to the power, one can write (for $R = R_{\texttt{probe}} + \frac{1}{T_2}$):

$$\texttt{Signal} \propto P_{\texttt{probe}} \times \phi_F \propto R_{\texttt{probe}} \times \frac{1}{R_{\texttt{probe}} + \frac{1}{T_2}} \tag{1.2.15}$$

Also, at the shot noise limit, where $\Delta\phi \propto 1/\sqrt{P_{\texttt{probe}}} \propto 1/\sqrt{R_{\texttt{probe}}}$, the sensitivity of the magnetometer will be:

$$\texttt{Sensitivity} = \frac{\Delta\phi}{|\partial\langle\phi\rangle/\partial B_y|} \propto \frac{1/\sqrt{R_{\texttt{probe}}}}{P_x} \propto \frac{R_{\texttt{probe}} + \frac{1}{T_2}}{\sqrt{R_{\texttt{probe}}}} \tag{1.2.16}$$

But as in any measuring device, what one actually wants is to maximize the signal to noise ratio:

$$\frac{\texttt{Signal}}{\texttt{Sensitivity}} \propto \frac{R_{\texttt{probe}}^{3/2}}{(R_{\texttt{probe}} + \frac{1}{T_2})^2} \tag{1.2.17}$$

from where it directly follows that $R_{\texttt{probe}} = 3 \times \frac{1}{T_2}$ and, since $R = R_{\texttt{probe}} + \frac{1}{T_2}$, $R = 4 \times \frac{1}{T_2}$. In more realistic conditions, the uncertainty in angle measurement, $\Delta\phi$, will not be shot noise limited and will generally be larger and not dependent on $R_{\texttt{probe}}$. In this case it turns out that `signal/sensitivity` is maximized for $R_{\texttt{probe}} = \frac{1}{T_2}$ and $R = 2 \times \frac{1}{T_2}$. In any case, the bandwidth of the magnetometer will be given by an equation of the form:

$$\omega_c = \frac{1}{T_2} + R + R_{\texttt{probe}} \simeq \frac{1}{T_2} \tag{1.2.18}$$

within a factor on the order of unity.

From the above follows that:

$$\partial\langle\phi\rangle/\partial B_y = \frac{\kappa\gamma}{\omega_c}\langle J_z\rangle \tag{1.2.19}$$

The inherent sources of noise, which cause the uncertainty in the rotation angle measurement, are the spin projection noise of the atoms, abbreviated *spn* from now on, and the fluctuations in the amplitude of the probe laser due to photon shot noise, *psn.* Therefore, since the two sources of noise are uncorrelated, their contributions to total noise are added in quadrature to yield:

$$\Delta\phi = \sqrt{\Delta\phi^2_{\mathtt{spn}} + \Delta\phi^2_{\mathtt{psn}}} \;\Rightarrow\; \Delta B_y = \sqrt{\Delta B^2_{y,\mathtt{spn}} + \Delta B^2_{y,\mathtt{psn}}} \tag{1.2.20}$$

We calculate the contributions from the two sources separately.

Spin Projection Noise

From equation (1.2.8) follows that $\Delta\phi_{\mathtt{spn}} = \kappa\Delta J_x$. So, from equations (1.2.27) and (1.2.19), we get:

$$\Delta B_{y,\mathtt{spn}} = \frac{\omega_c}{\gamma\sqrt{N}}\,\xi \tag{1.2.21}$$

where we have introduced the *spin squeezing parameter* [17] $\xi = \frac{\Delta J_x}{\sqrt{|\langle J_z\rangle|/2}}$. The uncertainty relation $\Delta J_x \Delta J_y \geq |\langle J_z\rangle|/2$, for an uncorrelated spin ensemble, for which $\Delta J_x = \Delta J_y$, leads to $\Delta J_x = \sqrt{|\langle J_z\rangle|/2}$ and, consequently to $\xi = 1$.

In an experiment, what we actually measure is the *power spectral density* (PSD) of the magnetic field in units of T/$\sqrt{\text{Hz}}$. The spn sensitivity in PSD units is given by dividing (1.2.21) with the square root of the bandwidth, $\sqrt{\omega_c}$, thus being[6]:

$$\delta B_{y,\mathtt{spn}} = \frac{1}{\gamma}\sqrt{\frac{\omega_c}{N}}\,\xi \tag{1.2.22}$$

Photon Shot Noise

The photon shot noise limited uncertainty in the measurement of angles with a polarimeter is given (see for example [3]):

$$\Delta\phi_{\mathtt{psn}} = \frac{1}{2\sqrt{\epsilon N_{\mathtt{tr}}}}\ \texttt{(in rad)} \tag{1.2.23}$$

---

[6] We use Δx for the normal variation of $\langle x\rangle$ and δx for the corresponding quantity in PSD units.

where $N_{\mathtt{tr}}$ is the transmitted number of photons through the cell reaching the photodetectors and ϵ is the quantum efficiency of the latter. In PSD units, N is replaced by the transmitted photon flux $\dot{N}_{\mathtt{tr}}$ and, thus:

$$\delta\phi_{\mathtt{psn}} = \frac{1}{2\sqrt{\epsilon \dot{N}_{\mathtt{tr}}}} \quad \texttt{(in}\ \mathrm{rad}/\sqrt{\mathrm{Hz}}\texttt{)} \tag{1.2.24}$$

So, the sensitivity limit due to psn is given directly in PSD units by:

$$\delta B_{y,\mathtt{psn}} = \frac{1}{\gamma}\sqrt{\frac{\omega_c}{N}}\,\eta \tag{1.2.25}$$

where after setting $\dot{N}_{\mathtt{tr}} = P_{\mathtt{inc}} e^{-N\sigma/A}/(hc/\lambda)$ with $P_{\mathtt{inc}}$ being the incident probe laser power,

$$\eta = \sqrt{\frac{(hc/\lambda)\omega_c N e^{N\sigma/A}}{4\epsilon P_{\mathtt{inc}}(\kappa\langle J_z\rangle)^2}} \simeq \sqrt{\frac{(hc/\lambda) N e^{N\sigma/A}}{4\epsilon P_{\mathtt{inc}} T_2(\kappa\langle J_z\rangle)^2}} \tag{1.2.26}$$

Total sensitivity due to physical sources

Adding equations (1.2.22) and (1.2.25) in quadrature, the total magnetic sensitivity in PSD units is obtained:

$$\delta B_y = \frac{1}{\gamma}\sqrt{\frac{\omega_c}{N}}\,\sqrt{\xi^2+\eta^2} \tag{1.2.27}$$

We note here that for uncorrelated spin ensembles it is $\xi = 1$, and for low vapor densities, $\eta \ll 1$. At these conditions, the formula above is simplified to $\delta B_y \simeq 1/\gamma\sqrt{NT_2}$, which is widely quoted in the bibliography. However, at high vapor densities, photon shot noise becomes important and has to be taken into account through the factor η.

- **Technical noise**

In actual experimental conditions, external noise, emanating mainly from ambient magnetic fields, usually dominates over inherent noise. Thus, when measuring extremely small magnetic fields it is necessary to shield the vapor cell from external magnetic fields. Magnetic shields used for this purpose are usually made of materials with very high magnetic permeability (permalloy, mu-metal, metglass etc). These shields isolate the sensor adequately from external fields, but they produce their own noise magnetic fields due to thermal Johnson currents running inside them. Although on the order of $1 - 10$ fT/$\sqrt{\text{Hz}}$, this kind of thermal noise dominates at low frequencies (up to a few kHz), but falls off at higher frequencies. Finally, another type of real-life noise in experiments is electronic noise in the electric circuits necessary for the acquisition of data, which nevertheless is usually negligible.

- **Total magnetic sensitivity**

Additional sources of noise, like thermal and electronic noise, are added in quadrature in equation (1.2.27), since they are uncorrelated with spn and psn. Thus, a more realistic formula for the magnetic sensitivity would be:

$$\delta B_y = \sqrt{\delta B^2_{y,\mathtt{spn}} + \delta B^2_{y,\mathtt{psn}} + \delta B^2_{y,\mathtt{th}} + \delta B^2_{y,\mathtt{e}}} \tag{1.2.28}$$

with the indices "`th`" and "`e`" standing for "thermal" and "electronic", respectively. Of these, thermal noise is particularly important, not only because it usually dominates over other sources, but also because it is of magnetic nature and it actually perturbs the measurement. In Chapter 3 we take advantage of this fact to raise the bandwidth of the EIT magnetometer proposed there above its TLA counterpart.

- **a numerical example**

To give a quick estimate of the various sources of noise, we cite the estimated thermal noise value from [1], where the authors, based on [16] and [13] for thermal magnetic noise in infinite conductive slabs, calculate the corresponding quantity for a five layer cylindrical shield similar to the one we are planning to use in our lab, claiming a value of $\delta B_{y,\mathtt{th}} \simeq 7$ fT/$\sqrt{\text{Hz}}$. The electronic noise is neglected in this example, so, to conclude the comparison, we calculate the spn and psn noise levels for a temperature $\theta = 150°\text{C}$. At this temperature, and assuming a cell length $l = 3$ cm and a probe beam diameter $w = 1$ cm, the number of interacting Rb atoms is calculated to be $N \simeq 10^{15}$. Also, ignoring diffusion, the transverse relaxation time is $T_2 \simeq 25$ ms. Thus, the spn noise, for $\gamma = 466$ kHz/G and $\omega_c = 4\times\frac{1}{T_2}$, will be $\delta B_{y,\mathtt{spn}} \simeq 0,07$ fT/$\sqrt{\text{Hz}}$. Finally, with a $P_{\mathtt{inc}} = 0,1$ mW probe beam tuned close to the D1 line of Rb at $\lambda = 795$ nm, it is found that the detuning which gives the best S/N will be $\delta \simeq 360\ \Gamma$, where $\Gamma = 2\pi \times 5,5$ MHz is the natural decay rate of Rb, and so, $\delta B_{y,\mathtt{psn}} \simeq 0,005$ fT/$\sqrt{\text{Hz}}$. The values calculated above clearly demonstrate the domination of thermal Johnson noise over other sources.

1.2.4 Density matrix approach

• definitions

The results obtained through the Bloch equations for the dynamics of the system under study can also be obtained through a more rigorous density matrix approach. Moreover, this is a step that must be taken in order to compare the TLA P-P magnetometer to the EIT-enhanced magnetometer we propose in the next chapter and for which the Bloch equations are not applicable.

We begin by defining the density matrix for the coupled TLA's of Fig. 1.1(b) [7]:

$$\rho = \begin{pmatrix} \rho_{\bar{g}\bar{g}} & \rho_{\bar{g}e} & \rho_{\bar{g}g} & \rho_{\bar{g}\bar{e}} \\ \rho^*_{\bar{g}e} & \rho_{ee} & \rho^*_{ge} & \rho^*_{\bar{e}e} \\ \rho^*_{\bar{g}g} & \rho_{ge} & \rho_{gg} & \rho_{g\bar{e}} \\ \rho^*_{\bar{g}\bar{e}} & \rho_{\bar{e}e} & \rho^*_{g\bar{e}} & \rho_{\bar{e}\bar{e}} \end{pmatrix} \tag{1.2.29}$$

We assume a DC magnetic field along $\hat{\boldsymbol{y}}$, with a Larmor frequency $\Omega_L = \gamma B_y$, and

---

[7] From now on, unless stated otherwise, $\hat{\boldsymbol{x}}$-axis will be considered as the quantization axis.

a probe field with a Rabi frequency $\Omega_p = \Omega e^{-i\omega t}$. It is convenient to work in the slowly varying matrix element picture, which is defined by the unitary transformations:

$$\tilde{\rho}_{\alpha\beta} \quad = \quad \rho_{\alpha\beta}\, e^{i\omega t} \qquad (\alpha = \bar{g}, g, \quad \beta = \bar{e}, e) \tag{1.2.30}$$

The interaction Hamiltonian in this picture is:

$$\mathcal{H} = \hbar \begin{pmatrix} \delta & \Omega & i\Omega_L & 0 \\ \Omega & 0 & 0 & -i\Omega_L \\ -i\Omega_L & 0 & \delta & \Omega \\ 0 & i\Omega_L & \Omega & 0 \end{pmatrix} \tag{1.2.31}$$

where $\delta = \omega_{ge} - \omega$ is the detuning of the probe beam, while we have also assumed that Ω is a real quantity, without loss of generality. Since we will always work in this picture, we drop the tilde and redefine $\tilde{\rho}_{\alpha\beta} \equiv \rho_{\alpha\beta}$. The evolution of the system will be described by the Liouville equation:

$$\frac{d}{dt}\rho = -\frac{i}{\hbar}[\mathcal{H}, \rho] + \mathcal{R}(\rho) \tag{1.2.32}$$

where the *relaxation matrix*, $R(\rho)$, is defined and discussed in Appendix B.

The procedure to be followed now is the following:

- First, in Appendix C, the equivalence between the density matrix approach and the Bloch equations is shown
- Secondly, in Appendix D, we establish the relation between the complex linear susceptibility of a medium and the density matrix elements. This is necessary in order to understand how solving for the density matrix determines the optical responce of the medium (dispersion and absorption) and points out the important matrix elements.

- Then we solve the steady state density matrix equations to acquire all quantities of interest

- Finally we redefine the magnetic sensitivity and the magnetometer signal in terms of the density matrix elements and these formulas will be used later in chapter 3 when we compare this type of magnetometer to its EIT counterpart.

• Steady state solution of the density matrix equations

The steady state solution of the Liouville equation (1.2.32) is reached in two steps. In the first step, we neglect the probe field and solve for the ground state matrix elements $\rho_{\bar{g}\bar{g}}$, ρ_{gg} and $\rho_{\bar{g}g}$. The solution yields, to the first order in the magnetic field:

$$\begin{aligned} \rho_{\substack{\bar{g}\bar{g}\\ gg}} &= \frac{1}{2} \pm \frac{R\,\Omega_L}{(1/T_2+R)^2} = \frac{1}{2} \pm \frac{T_2\Omega_L}{4} \\ \rho_{\bar{g}g} &= \frac{R}{2(1/T_2+R)} = -\frac{1}{4} \end{aligned} \tag{1.2.33}$$

where the rightmost values are for $R = \frac{1}{T_2}$, which is the optical pumping rate value that optimizes the TLA pump-probe magnetometer, as mentioned earlier. In the second step of the calculation, the elements $\rho_{\bar{g}e}$ and $\rho_{g\bar{e}}$ are obtained for constant $\rho_{\bar{g}\bar{g}}$, ρ_{gg} and $\rho_{\bar{g}g}$. That is to say that the probe field is considered weak enough so as not to perturb the populations, which is half-true but nevertheless a common and adequate approximation. The obtained solution is kept in first order in the probe Rabi frequency and has the familiar form:

$$\rho_{\substack{\bar{g}e\\ g\bar{e}}} = \Omega\rho_{\substack{\bar{g}\bar{g}\\ gg}}\,\frac{\delta + i\,\Gamma/2}{\delta^2 + (\Gamma/2)^2} \tag{1.2.34}$$

where the magnetic field dependence is hidden in the populations $\rho_{\bar{g}\bar{g}}$ and ρ_{gg} given in eq.(1.2.33).

1.2.5 Sensitivity and Signal in the density matrix approach

- **Paramagnetic Faraday effect and Signal of the magnetometer**

Having mentioned the paramagnetic Faraday effect in §1.2.1 and §1.2.2, we return to see how it is explained physically and to connect the rotation angle to the density matrix. The probe field in a pump-probe magnetometer is linearly polarized, as mentioned earlier, and can thus be split in a right-circularly polarized (σ^+) and a left-circularly polarized (σ^-) component. The σ^+ and σ^- components probe the $|\bar{g}\rangle \rightarrow |e\rangle$ and $|g\rangle \rightarrow |\bar{e}\rangle$ transitions, respectively. Dispersion and absorption of a beam propagating in a certain direction are determined by the real and imaginary parts of the refractive index, n' and n'', respectively, or, equivalently, of the linear susceptibility, χ' and χ''. This can be seen as follows: if the electric field of a beam propagating along, say, $\hat{\boldsymbol{x}}$ has a dependance of the form e^{ikx}, with $k = \frac{2\pi n}{\lambda}$, then this dependence can be written as $\exp(\frac{i2\pi n' x}{\lambda})\exp(-\frac{2\pi n'' x}{\lambda})$. Thus the beam accumulates phase with a spatial rate $\frac{i2\pi n'}{\lambda} \propto n'$ (dispersion) and attenuates with an absorption coefficient $\frac{2\pi n''}{\lambda} \propto n''$ (absorption). Since the magnetic field slightly perturbs the populations of the ground state levels, it also induces small discrepancies between the refraction indices experienced by the σ^+ and σ^- fields, which means that as the two fields propagate through the vapor, they acquire different phase shifts and the polarization plane of the linear polarized field at the exit of the vapor cell will be rotated with regard to the incident beam polarization plane. This is the *paramagnetic Faraday effect* and the rotation angle of the polarization plane is termed *the Faraday rotation angle.* So, if a length l is traversed through the vapor by the two fields, their phase difference will be equal to (two times) the Faraday rotation angle of the polarization plane of the probe, ϕ_F:

$$\phi_F = \frac{1}{2}\frac{2\pi l}{\lambda}\left(n'_{(+)} - n'_{(-)}\right) = \frac{\pi l}{2\lambda}\left(\chi'_{(+)} - \chi'_{(-)}\right) \tag{1.2.35}$$

Since $\chi_{(\pm)}$ is proportional to $\rho_{\substack{\bar{g}e \\ g\bar{e}}}$, using equation (D.0.9) the Faraday rotation angle is related to the density matrix:

$$\phi_F = \frac{3n_d\lambda^2 l}{16\pi\tilde{\Omega}}\left[\Re(\rho_{\bar{g}e}) - \Re(\rho_{g\bar{e}})\right] \tag{1.2.36}$$

The signal of the magnetometer will be given by equation (1.2.2), which we rewrite:

$$S = 2\phi_F I_{\mathtt{tr}} = 2\phi_F I_o e^{-\alpha l}$$

In the density matrix approach, α is given by:

$$\alpha = \frac{2\pi n''}{\lambda} = \frac{3n_d\lambda^2}{8\pi\tilde{\Omega}}|\Im(\rho_{ge}^{(o)})| \tag{1.2.37}$$

with the assumption that $\Im(\rho_{\bar{g}e}) \simeq \Im(\rho_{g\bar{e}}) \simeq \Im(\rho_{ge}^{(o)})$ [8].

• alternative expressions for ϕ_F and α

The above relations are general and will be used for both the TLA and EIT magnetometer. However, especially for the TLA case we can use equations (1.2.33) and (1.2.34) to express the rotation angle and absorption coefficient in terms of the ground state populations and, ultimately, in terms of the applied magnetic field. So, in terms of populations, we obtain:

$$\begin{aligned} \texttt{vs populations:} \quad \phi_F &= \frac{3n_d\lambda^2 l}{8\pi}\frac{\delta(\Gamma/2)}{\delta^2+(\Gamma/2)^2}\left(\rho_{\bar{g}\bar{g}} - \rho_{gg}\right) \\ \alpha &= \frac{3n_d\lambda^2}{4\pi}\frac{(\Gamma/2)^2}{\delta^2+(\Gamma/2)^2}\,\rho_{gg}^{(o)} \end{aligned} \tag{1.2.38}$$

and after substituting the populations from equations (1.2.33):

$$\begin{aligned} \texttt{vs magnetic field:} \quad \phi_F &= \frac{3n_d\lambda^2 l}{16\pi}\frac{\delta(\Gamma/2)}{\delta^2+(\Gamma/2)^2}T_2\Omega_L \\ \alpha &= \frac{3n_d\lambda^2}{8\pi}\frac{(\Gamma/2)^2}{\delta^2+(\Gamma/2)^2} \end{aligned} \tag{1.2.39}$$

---

[8] Note: $\rho_{ge}^{(o)}$ is the unperturbed by the magnetic field element for the $\sigma^{\pm}$ transitions. Obviously, in the absence of the magnetic field $\Im(\rho_{\bar{g}e}) = \Im(\rho_{g\bar{e}}) = \Im(\rho_{ge}^{(o)})$ due to symmetry

We note here that, for large detunings, absorption scales as $1/\delta^2$ while ϕ_F scales as $1/\delta$. It is thus advantageous for TLA magnetometers to be operated at large detunings, where the relations above are approximated by:

$$\begin{aligned} \texttt{for large detunings:} \quad \phi_F &= \frac{3n_d\lambda^2 l}{32\pi}\,\frac{\Gamma}{\delta}\,T_2\Omega_L \\ \alpha &= \frac{3n_d\lambda^2}{32\pi}\,\frac{\Gamma^2}{\delta^2} \end{aligned} \tag{1.2.40}$$

- **Magnetic sensitivity**

The magnetic sensitivity must also be expressed in terms of the density matrix. The fundamental sensitivity is given by equation (1.2.27), which we rewrite as:

$$\delta B = \frac{\sqrt{\omega_c}}{\gamma\sqrt{N}}\sqrt{\xi^2+\eta^2} = \delta B_\circ\sqrt{\xi^2+\eta^2}$$

The only factor related to the density matrix is the photon shot noise factor, η, which contains the exponent indicating absorption of the probe beam and which is now expressed as:

$$\eta = \sqrt{\frac{(hc/\lambda)\omega_c N e^{\alpha l}}{4\epsilon P_{\texttt{inc}}(\kappa\langle J_z\rangle)^2}} \tag{1.2.41}$$

with α generally given by equation (1.2.37) or by any of the equations (1.2.38) through (1.2.40) for the TLA magnetometer case.

Chapter 2

E.I.T. and L.W.I. basics

Before we present our proposal for a high-bandwidth magnetometer, the physical concepts underlying Electromagnetically Induced Transparency (E.I.T.) and Lasing (or Amplification) Without Inversion (L.W.I. or A.W.I.) have to be explained.

2.1 E.I.T. basics

The abbreviation "E.I.T." stands for ***E**lectromagnetically **I**nduced **T**ransparency* and it implies the conditions under which a medium becomes transparent to a coherent electromagnetic field at some frequency. It is worth mentioning that the first publications about EIT (Kocharovskaya and Khanin in 1988 [10] and, independently, Harris in 1989 [9]) were concerned with the possibility of Lasing Without Inversion (L.W.I.) rather than with EIT in itself[1]. The name is due to a subsequent paper by S. Harris [8]. To create EIT conditions two distinct transitions of an atomic medium have to be stimulated, which must involve one common state. The stimulation of the two transitions, depending on the particular setup, can be achieved by one or two coherent fields. Depending on the configuration of the atomic states involved, EIT

---

[1] Lately, reprints of old Russian articles regarding EIT and LWI, authored mainly by A.K. Popov and dating back to the late 60s, have appeared in the Los Alamos preprint server (http://www.lanl.gov). It is, however, highly unlikely that Dr. Popov will be remembered as the father and inventor of these phenomena (paper numbers: $\mathrm{quant-ph}/0005042, ...049, ...060, ...081, ...089, ...094, ...108, ...114, ...118$. Info source: David Mc Gloin PhD thesis [5])

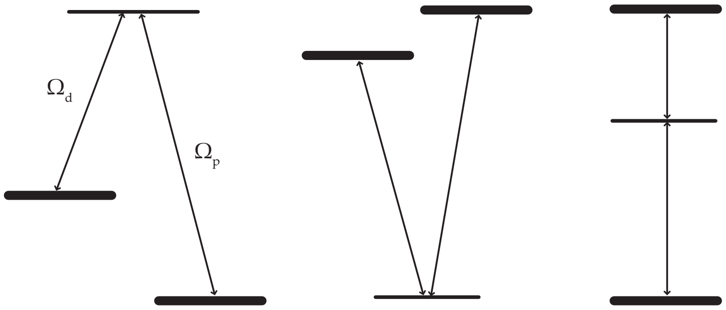

Figure 2.1: EIT is possible in Λ, V and Ξ systems. In any case states of the same parity (thick lines) are coupled to produce EIT conditions, while the opposite parity state (thin lines) is eliminated.

can be achieved in any of the Λ, V or Ξ (a.k.a. Ladder) systems shown in Figure 2.1, with varying efficiency. The idea behind EIT is that atoms, through the simultaneous interaction with the two coherent fields, are pumped into a state which is a coherent superposition of the two states with the same parity, while the different parity state is effectively shielded out and never populated. The physical explanation of the phenomenon is that an atom in this state only undergoes two-photon procedures (absorption of a photon from one beam and stimulated re-emission in the other beam and vice versa) effectively never absorbing light from any of the fields. This is why this state is commonly called a *dark state*. Thus, pumping the atoms of a medium into such a state creates the appropriate conditions for - at least the weakest of the two [2] - fields to propagate without absorption, rendering the medium *transparent*. The two fields used are called *probe* and *drive* (or *coupling*) fields, and their Rabi frequencies will be denoted as Ω_p and Ω_d, respectively (as in Fig.2.1). The usual case is that we are interested in obtaining transparency for the probe field and will generally use a quite stronger drive field to prepare the conditions. In the following we describe EIT and LWI through a density matrix approach, using a simple 3-level system in the Λ configuration.

---

[2] If one of the two fields is much stronger than the other, then it has to be turned on before the weak one so as to saturate its transition. This way the medium will also be transparent to it, since in EIT there will be no actual repopulation of the ground state of the strong field transition

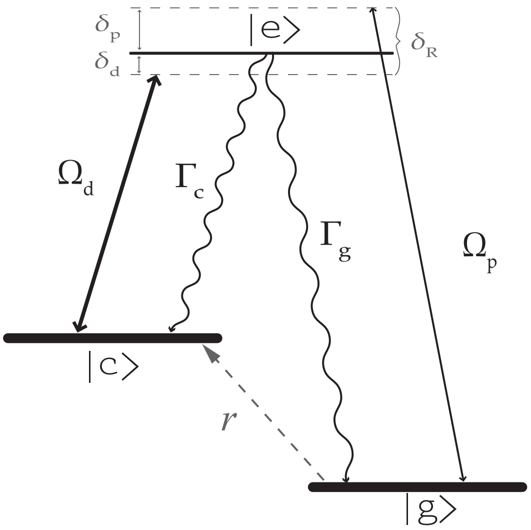

Figure 2.2: Λ system: fields, decays, relaxations and maybe a small pumping rate that leads to L.W.I.

a density matrix approach to EIT

In Figure 2.2 a simple Λ system is depicted. The probe and drive fields are acting on the transitions $|g\rangle \leftrightarrow |e\rangle$ and $|c\rangle \leftrightarrow |e\rangle$, respectively. The excited state $|e\rangle$ decays back to states $|g\rangle$ and $|c\rangle$ with rates Γ_g and Γ_c, respectively, with the total decay rate of the excited state being $\Gamma = \Gamma_g + \Gamma_c$. We will hereby assume, with minimum loss of generality, that $\Gamma_g = \Gamma_c = \Gamma/2$. An important feature of the system that allows the phenomena we are about to discuss to appear, is that both $|g\rangle$ and $|c\rangle$ states are long lived, metastable or stable states, that is the population decay rates of these states is negligible in comparison to the decay rate of the excited state. Finally, any coherence created between states $|g\rangle$ and $|c\rangle$ is decaying with a small decoherence rate γ_{gc}. For the moment we ignore the rate r appearing in Fig. 2.2, which pumps population from state $|g\rangle$ to $|c\rangle$. We will return to see how such a small rate can lead to amplification of the probe beam, without inversion of populations.

Working directly with the slowly varying matrix elements (as in 1.2.4) we express the density matrix, the Hamiltonian and the relaxation matrix for the Λ system as follows:

$$\rho = \begin{pmatrix} \rho_{gg} & \rho_{ge} & \rho_{gc} \\ \rho_{ge}^* & \rho_{ee} & \rho_{ce}^* \\ \rho_{gc}^* & \rho_{ce} & \rho_{cc} \end{pmatrix} \tag{2.1.1}$$

$$\mathcal{H} = \hbar \begin{pmatrix} \delta_p & \Omega_p & 0 \\ \Omega_p^* & 0 & \Omega_d^* \\ 0 & \Omega_d & \delta_d \end{pmatrix} \tag{2.1.2}$$

$$\mathcal{R}(\rho) = \begin{pmatrix} \frac{\Gamma}{2}\rho_{ee} & -\frac{\Gamma}{2}\rho_{ge} & -\gamma_{gc}\rho_{gc} \\ -\frac{\Gamma}{2}\rho_{ge}^* & -\Gamma\rho_{ee} & -\frac{\Gamma}{2}\rho_{ce}^* \\ -\gamma_{gc}\rho_{gc}^* & -\frac{\Gamma}{2}\rho_{ce} & \frac{\Gamma}{2}\rho_{ee} \end{pmatrix} \tag{2.1.3}$$

The system obeys the Liouville equation, $\frac{d}{dt}\rho = -\frac{i}{\hbar}[\mathcal{H}, \rho] + \mathcal{R}(\rho)$, which we solve for the steady state, i.e. setting $\frac{d\rho}{dt} = 0$. The important part of the solution is the element ρ_{ge} which is related to the absorption and dispersion of the probe beam (see §1.2.4):

$$\rho_{ge} \simeq \frac{\left[\left(\frac{\Gamma}{2} - i\delta_d\right)\rho_{gg} - \frac{\Omega_d^2}{\gamma_{gc}+i\delta_R}\rho_{cc}\right] i\Omega_p}{\left(\frac{\Gamma}{2} - i\delta_d\right)\left(\frac{\Gamma}{2} + i\delta_p + \frac{\Omega_d^2}{\gamma_{gc}+i\delta_R}\right)} \simeq \frac{i\Omega_p\rho_{gg}}{\frac{\Gamma}{2} + i\delta_p + \frac{\Omega_d^2}{\gamma_{gc}+i\delta_R}} \tag{2.1.4}$$

where $\delta_R = \delta_p - \delta_d$ is the so called *Raman detuning.* Also, the rightmost part of eq.(2.1.4) is valid for $\Omega_p \ll \Omega_d$, that is when the drive field is much stronger than the probe. In this case the probability for an atom to be found in the ground state, $|g\rangle$, from where it is supposed to have originated, is much higher than for the intermediate state, $|c\rangle$ (i.e. $1 \simeq \rho_{gg} \gg \rho_{cc} \simeq 0$).

The real and imaginary parts of ρ_{ge} are plotted with solid lines in Fig. 2.3 versus the Raman detuning for some typical parameter values. Along with them, the dotted lines show the respective TLA response. We first focus on the case where the detuning of the drive beam, δ_d, is zero. In this case the drive beam is continuously resonant with the $|c\rangle \leftrightarrow |e\rangle$ transition and the Raman detuning coincides with the probe detuning, $\delta_R = \delta_p$. As mentioned in §1.2.4 the imaginary part of ρ_{ge} determines the absorption of the beam stimulating the $|g\rangle \leftrightarrow |e\rangle$ transition through eq.(D.0.7). Looking at the

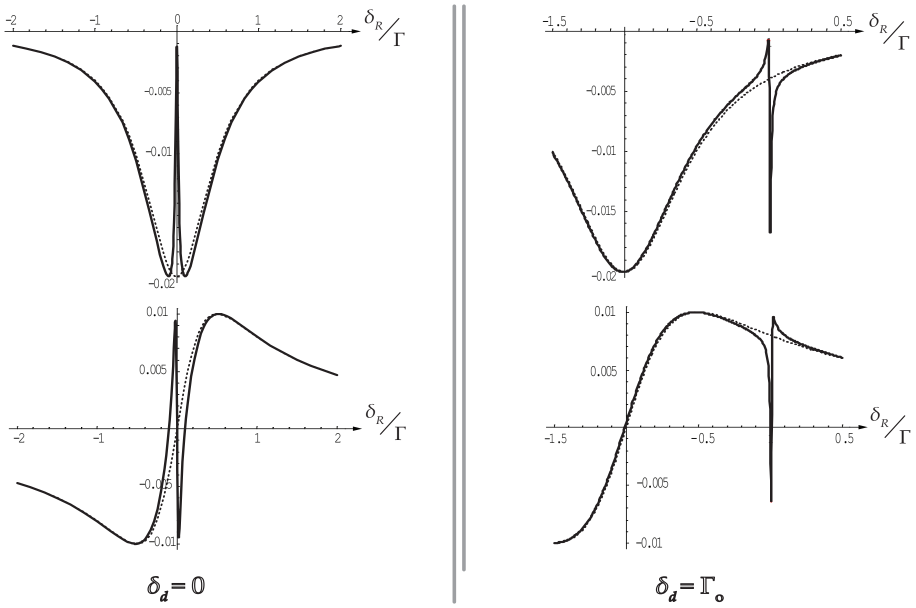

Figure 2.3: Imaginary (top) and Real (bottom) parts of ρ_{ge} vs the Raman detuning, for $\delta_d = 0$ and for $\delta_d \neq 0$ (here $\delta_d = \Gamma$) . Dotted lines are the corresponding elements for a Two Level Atom. Parameter values: $\Omega_d = 10\Omega_p = 0.1\Gamma$, $\gamma_{gc} = 0.001\Gamma$

TLA response in Fig. 2.3 (top left/dotted line) we see, as expected, the absorption getting larger as the frequency of the beam approaches the resonant frequency of the transition and being maximized exactly on resonance. Now turning on the drive field and tuning it on resonance with the $|c\rangle \leftrightarrow |e\rangle$ transition we see that the probe behavior changes (top left/solid line). Still, as its frequency approaches resonance, its absorption becomes larger, but near the resonance the absorption peak splits into two distinct peaks and for a small *window* of frequencies (called the *transparency window*) between these peaks its absorption practically vanishes, becoming *minimum* exactly on resonance Then, the probe beam propagates through the medium without attenuation. This behavior is due to the fact that, under these conditions, atoms are pumped into the non-absorbing dark state comprised of the states $|g\rangle$ and $|c\rangle$, which is long-lived, provided that any decay and decoherence rates associated with these states are quite small compared to Ω_d.

A fact of equal importance for most practical applications is that near resonance the probe experiences steep, normal and linear dispersion (bottom left/solid line in Fig.2.3) the slope of which is determined by the drive field strength (the lower Ω_d is, the steeper the dispersion). Thus, under EIT conditions, it is possible for the probe to acquire large phase shifts at minimum absorption, a characteristic which gives rise to many novel phenomena such as ultra-slow pulse group velocities, storage of light and, of course, large Faraday rotations, which will be a key feature of the magnetometer scheme we propose later on.

We now turn to the case where $\delta_d \neq 0$ (right column in Fig.2.3). We see that near the $|g\rangle \leftrightarrow |e\rangle$ transition resonance the probe behaves *almost* like it would in a TLA, but this statement becomes less and less accurate as the drive Rabi frequency becomes larger, since for larger drive intensities Stark shifts of the single-photon probe resonance become important. However, near the Raman resonance, $\delta_R = 0$, the EIT conditions are fulfilled. Once again a steep feature appears in both the absorption and dispersion profiles, with absorption being minimum and the refractive index taking its vacuum value exactly on Raman resonance.

2.2 L.W.I. basics

We now go back to Fig. 2.2, but this time we also take into account the small incoherent rate r at which population is transferred from state $|g\rangle$ to state $|c\rangle$. We note here that, since the two states have the same parity, this rate can not be achieved by some incoherent light source pumping population directly from $|g\rangle$ to $|c\rangle$. However, an incoherent beam pumping population from $|g\rangle$ to $|e\rangle$ can do the trick since some of the pumped population will end up in state $|c\rangle$, thus providing an *effective* pumping rate r from $|g\rangle$ to $|c\rangle$. We generally impose the condition that $r \ll \Gamma$.

The system obeys the Liouville equation, with the relaxation matrix (2.1.3) modified to include the effect of the $|g\rangle \rightarrow |c\rangle$ pumping:

$$\mathcal{R}(\rho) = \begin{pmatrix} -r\rho_{gg} + \frac{\Gamma}{2}\rho_{ee} & -(\frac{\Gamma+r}{2})\rho_{ge} & -(\frac{r}{2}+\gamma_{gc})\rho_{gc} \\ -\frac{\Gamma+r}{2}\rho_{ge}^{*} & -\Gamma\rho_{ee} & -\frac{\Gamma}{2}\rho_{ce}^{*} \\ -(\frac{r}{2}+\gamma_{gc})\rho_{gc}^{*} & -\frac{\Gamma}{2}\rho_{ce} & r\rho_{gg} + \frac{\Gamma}{2}\rho_{ee} \end{pmatrix} \tag{2.2.1}$$

and the steady state element ρ_{ge} is now given by:

$$\rho_{ge} \simeq \frac{\left[\left(\frac{\Gamma}{2} - i\delta_d\right)\rho_{gg} - \frac{\Omega_d^2}{\frac{r}{2}+\gamma_{gc}+i\delta_R}\ \rho_{cc}\right] i\Omega_p}{\left(\frac{\Gamma}{2} - i\delta_d\right)\left(r + \frac{\Gamma}{2} + i\delta_p + \frac{\Omega_d^2}{\frac{r}{2}+\gamma_{gc}+i\delta_R}\right)} \tag{2.2.2}$$

where:

$$\rho_{gg} \simeq \frac{\frac{\Gamma+r}{2}\ \Omega_d^2}{r\left[\left(\frac{\Gamma}{2}\right)^2 + \delta_d^2\right] + \left(2\ r + \frac{\Gamma}{2}\right)\ \Omega_d^2} \simeq 1 - \rho_{cc} \gg \rho_{ee} \tag{2.2.3}$$

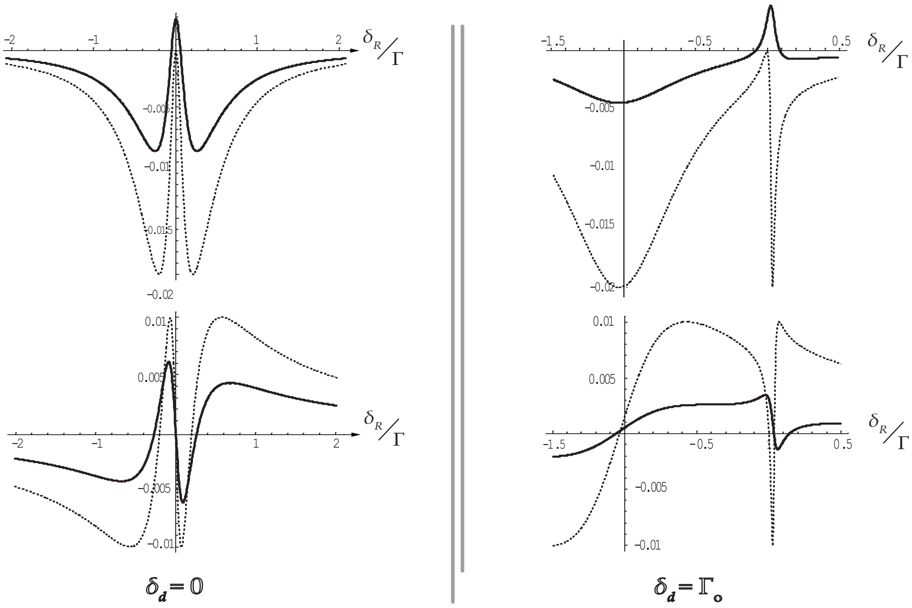

$\delta_d = 0$

$\delta_d = \Gamma_o$

Figure 2.4: Imaginary (top) and Real (bottom) parts of ρ_{ge} vs the Raman detuning, for $\delta_d = 0$ and for $\delta_d \neq 0$ (here $\delta_d = \Gamma$) . Dotted lines are the corresponding elements for the normal E.I.T. case. Parameters: $\Omega_d = 20\Omega_p = 0.2\Gamma$, $\gamma_{gc} = 0.001\Gamma$, $r = 0.05\Gamma$

In Figure 2.4 we plot ρ_{ge} from eq.(2.2.2) [solid lines] along with ρ_{ge} from eq.(2.1.4) of the normal EIT case [dotted lines]. The first remark is that, since ρ_{cc} is not negligible in this case, ρ_{gg} will be smaller than in the simple EIT case. Thus both the absorption and dispersion curves, which scale with ρ_{gg}, will have lower peak values, something that is evident in the Figure, and so, the dispersion in the vicinity of the Raman resonance will be less steep than before.

But there is another, somewhat unexpected, behavior evident in Figure 2.4. If the rate r is greater than some critical value, a region of *positive absorption*, that is *amplification*, appears around the Raman resonance. This means that the probe beam, if properly tuned, will not only pass through the medium with no attenuation, but, on the contrary, it will be amplified, even though there is no population inversion between states $|g\rangle$ and $|e\rangle$. This is why this effect is called *Lasing* (or *Amplification*) *Without Inversion* (LWI or AWI). An experimental demonstration of this effect is presented in [18].

In a quite loose quantum-optical notation, the EIT and LWI procedures can be put in the schematic form:

$$\begin{array}{lccccc}
\text{EIT} & |g,\ n_p,\ n_d\rangle & \rightarrow & |c,\ n_p-1,\ n_d+1\rangle & \rightarrow & |g,\ n_p,\ n_d\rangle \\
\text{LWI} & |g,\ n_p,\ n_d\rangle & -\,[r]\rightarrow & |c,\ n_p,\ n_d\rangle & \rightarrow & |g,\ n_p+1,\ n_d-1\rangle
\end{array}$$

where in the brackets the atomic state ($|g\rangle$ or $|c\rangle$) and the probe and drive beam photons (n_p and n_d, respectively) are denoted[3]. From this table it becomes obvious that although there is no inversion, there is also no magic in the amplification of the probe beam: what the probe beam gains, the drive beam loses and if any extra energy is required, it is also provided externally by the $|g\rangle \rightarrow |c\rangle$ pumping procedure.

---

[3] This notation is used in quantum optics where both the atomic system and the electromagnetic fields are quantized. If an atom is in the atomic state $|x\rangle$ and interacts with a photon number state $|n\rangle$ (that is an eigenstate of the quantized electromagnetic field with zero uncertainty in the number of photons), then the state of this fully quantized system is $|x\rangle \otimes |n\rangle$ or, to save notation, $|x\ ,n\rangle$.

A note on the validity of the discussion above

The results obtained in this section are to be treated with caution, since on one hand they were arrived at by treating the probe field linearly, assuming $\Omega_p \ll \Omega_d$, on the other hand the effect involves amplification of the probe. This means that our conclusions are of limited applicability and will definitely become invalid once the amplitude of the probe becomes comparable to the amplitude of the drive. Moreover, as the probe is being amplified, non-linear phenomena are becoming more important and can not be neglected. However, as long as one keeps the probe in the non-amplifying regions, eq.(2.2.2) and the discussion following its derivation remain valid.

For a general discussion on EIT and related applications see the classic review by E. Arimondo [2] and a more recent one by M. Fleischhauer, A. Imamoglu and J.P. Marangos [4].

2.3 The merits of Λ-systems

In the following Chapter we propose using Λ-system atoms in order to enhance the performance of a pump-probe magnetometer. For an atomic magnetometer system there are two principal demands on the atomic medium used:

- **low absorption**, because the sensitivity of the magnetometer depends on the flux of probe photons reaching the detectors after traversing the medium
- **large and steep dispersion**, because the signal of the magnetometer is proportional to the Faraday rotation angle of the probe, which is in turn determined by the dispersion.

A Λ-system medium can achieve both. In particular, in an A.W.I. system one can tune the probe beam to achieve *zero* absorption, still maintaining large dispersion, making it an ideal candidate for an atomic magnetometer.

Chapter 3

High - Bandwidth Magnetometer with an E.I.T. probe

3.1 Introduction

In this Chapter we study the high bandwidth atomic magnetometer setup proposed in this thesis. The medium used in the description of the operational principle is actually a *toy model* of a fictitious atom with $J = \frac{1}{2}$ ground, excited and intermediate states. Each of these states is split into two $M = \pm\frac{1}{2}$ Zeeman substates. An incoherent pump beam, propagating along $\hat{\boldsymbol{z}}$, produces a $\hat{\boldsymbol{z}}$-polarization, which is slightly rotated around $\hat{\boldsymbol{y}}$-axis by a weak magnetic field, $\boldsymbol{B}$, which lies on the $\hat{\boldsymbol{y}}$-axis. The medium is illuminated by two linearly polarized coherent fields, the probe and the drive, co-propagating along $\hat{\boldsymbol{x}}$, and each atom behaves as a pair of Λ-systems coupled by the magnetic field, as in Figure 3.1. The magnetic field is determined by the Faraday rotation angle of the probe field passing through the medium.

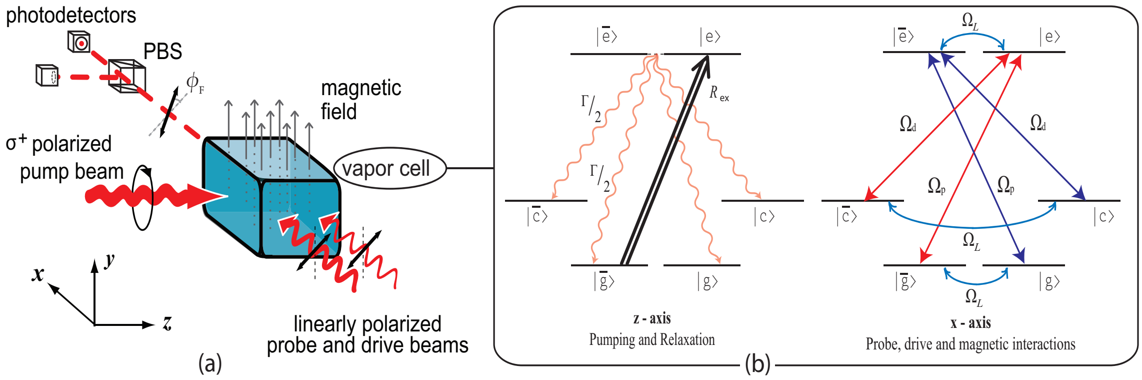

Figure 3.1: The proposed EIT-enhanced magnetometer model has a strong linearly polarized *drive* beam copropagating with the probe

3.2 Density matrix treatment

3.2.1 Steady state solution of the Liouville equation

The proposed scheme is studied under a density matrix formulation so that it can be directly compared to the TLA pump-probe magnetometer treated similarly in subsection 1.2.4. The density matrix of the system is given by:

$$\rho = \begin{pmatrix} \rho_{\bar{g}\bar{g}} & \rho_{\bar{g}e} & \rho_{\bar{g}\bar{c}} & \rho_{\bar{g}g} & \rho_{\bar{g}\bar{e}} & \rho_{\bar{g}c} \\ \rho^*_{\bar{g}e} & \rho_{ee} & \rho^*_{\bar{c}e} & \rho^*_{ge} & \rho^*_{\bar{e}e} & \rho^*_{ce} \\ \rho^*_{\bar{g}\bar{c}} & \rho_{\bar{c}e} & \rho_{\bar{c}\bar{c}} & \rho^*_{g\bar{c}} & \rho_{\bar{c}\bar{e}} & \rho_{\bar{c}c} \\ \rho^*_{\bar{g}g} & \rho_{ge} & \rho_{g\bar{c}} & \rho_{gg} & \rho_{g\bar{e}} & \rho_{gc} \\ \rho^*_{\bar{g}\bar{e}} & \rho_{\bar{e}e} & \rho^*_{\bar{c}\bar{e}} & \rho^*_{g\bar{e}} & \rho_{\bar{e}\bar{e}} & \rho^*_{c\bar{e}} \\ \rho^*_{\bar{g}c} & \rho_{ce} & \rho^*_{\bar{c}c} & \rho^*_{gc} & \rho_{c\bar{e}} & \rho_{cc} \end{pmatrix} = \begin{pmatrix} [\ \rho_{\Lambda_1}\ ] & [\rho_{\Lambda_{12}}] \\ [\rho^*_{\Lambda_{12}}] & [\ \rho_{\Lambda_2}\ ] \end{pmatrix} \tag{3.2.1}$$

where the $[\rho_{\Lambda_{1\ \text{or}\ 2}}]$ refer to the 3×3 matrices corresponding to the $|\bar{g}\rangle - |e\rangle - |\bar{c}\rangle$ or $|g\rangle - |\bar{e}\rangle - |c\rangle$ Λ-system and $[\rho_{\Lambda_{12}}]$ to the 3×3 matrix containing the mixing elements between the two Λ-systems. All elements in $\rho_{\Lambda_{12}}$ should be zero if the two Λ-systems were completely decoupled.

In the slowly varying matrix element picture, the Hamiltonian of the system is:

$$\mathcal{H}=\begin{pmatrix} \delta_p & \Omega_p & 0 & i\Omega_L & 0 & 0 \\ {\Omega_p}^* & 0 & {\Omega_d}^* & 0 & -i\Omega_L & 0 \\ 0 & \Omega_d & \delta_d & 0 & 0 & i\Omega_L \\ -i\Omega_L & 0 & 0 & \delta_p & \Omega_p & 0 \\ 0 & i\Omega_L & 0 & {\Omega_p}^* & 0 & {\Omega_d}^* \\ 0 & 0 & -i\Omega_L & 0 & \Omega_d & \delta_d \end{pmatrix} = \begin{pmatrix} [\mathcal{H}_{\Lambda_1}] & [\mathcal{H}_{\Lambda_{12}}] \\ [\mathcal{H}^*_{\Lambda_{12}}] & [\mathcal{H}_{\Lambda_2}] \end{pmatrix} \tag{3.2.2}$$

where we see that the two Λ-systems are formed due to the interaction with the $\mathcal{H}_{\Lambda_1 \text{ or } 2}$ Hamiltonians and are mixed through the magnetic field contained in $\mathcal{H}_{\Lambda_{12}}$. The evolution of the system is described by the Liouville equation (1.2.32), with the relaxation matrix, $\mathcal{R}(\rho)$, defined in Appendix B.

Following the definitions of the various matrices, the Liouville equation has to be solved for the steady state. However, the complete solution in this case is rather abstruse and greatly obscures the underlying physics. Thus the solution is obtained in two steps, each based on some reasonable simplifying assumption, the ultimate target being to arrive at results which will clarify the physics of the system while being as simple as possible, albeit not inaccurate.

Solution step 1

The first step towards the final solution of the Liouville equation is to solve it in the absence of the probe field. In this way the steady state populations of the atomic states are calculated versus the pumping rate, R, the drive field Rabi frequency, Ω_d, and the Larmor frequency, Ω_L. The idea here is that the probe field is what its name denotes: a probe. It *probes* a set situation without perturbing the system. Physically this means that the probe field is weak enough so that its effect can be neglected.

So in the absence of the probe field and taking into account only linear terms in the magnetic field, the following results are obtained:

$$\begin{aligned}
\rho_{\substack{\bar{g}\bar{g}\\gg}} &\simeq \rho^{(\circ)}_{gg}\left(1 + {f_g}^2\frac{\Omega_L}{R_{\mathtt{eff}}}\right) &\rightarrow\quad & \rho^{(\circ)}_{gg}\left(1 \pm \frac{\Omega_L}{2/T_2}\right) \\
\rho_{\substack{\bar{c}\bar{c}\\cc}} &\simeq \rho^{(\circ)}_{cc} = f_c(s)\ \rho^{(\circ)}_{gg} &\rightarrow\quad & \frac{3}{2}\ \frac{s}{s+1}\ \rho^{(\circ)}_{gg} \qquad (3.2.3) \\
\rho_{\bar{g}g} &\simeq \rho^{(\circ)}_{\bar{g}g} = f_g\rho^{(\circ)}_{gg} &\rightarrow\quad & \frac{1}{2}\ \rho^{(\circ)}_{gg}
\end{aligned}$$

where

$$f_g = \frac{2R_{\mathtt{eff}}}{\frac{1}{T_2} + 2R_{\mathtt{eff}}} \quad \text{and} \quad f_c(s) = \frac{\frac{1}{T_2} + 4R_{\mathtt{eff}}}{\frac{1}{T_2} + 2R_{\mathtt{eff}}}\ \frac{s}{s+1} \quad \text{with} \quad s = \frac{\Gamma^2/4 + \delta_d^2}{T_2\Gamma\Omega_d^2} \qquad (3.2.4)$$

and the zero magnetic field populations $\rho^{(\circ)}_{gg}$ of states $|g\rangle$ or $|\bar{g}\rangle$ are given by:

$$\rho^{(\circ)}_{gg} \simeq \frac{1}{4}\left(1 \pm \frac{1 - \frac{2R_{\mathtt{eff}}}{1/T_2 + 2R_{\mathtt{eff}}}s}{1 + 2\ \frac{1/T_2 + 3R_{\mathtt{eff}}}{1/T_2 + 2R_{\mathtt{eff}}}}\right) \rightarrow \frac{1}{4}\left(1 + \frac{1 - s/2}{1 + (5/2)s}\right) \qquad (3.2.5)$$

where $R_{\mathtt{eff}} = R_{\mathtt{ex}}/4$ (see Appendix B). Two important facts have to be noted here. The first one is that in all cases the values after the arrows assume an excitation rate $R_{\mathtt{ex}} = 2 \times \frac{1}{T_2}$ and constitute a special case of the general results. The reason for this selection is obviously the ability to compare this magnetometer setup to the TLA pump-probe magnetometer, which is optimized for that value of $R_{\mathtt{ex}}$. However, optimization in our case is a 3-parameter procedure, the parameters being, apart from the excitation rate, $R_{\mathtt{ex}}$, the drive field Rabi frequency, Ω_d, and the drive field detuning, δ_d, which effectively determines the position of the Raman resonance. It is thus in principle possible for such a magnetometer to operate equally well for various interrelated sets of these 3 parameters. The second thing is that we have given above the magnetic field dependence only for the ground states, while neglecting this dependence for the other matrix elements, the reason for this being of course that this is the dominating magnetic term.

Solution step 2

In this step, the probe field is restored and the Liouville equations are solved, but with $\rho_{\substack{\bar{g}\bar{g}\\ gg}}$, $\rho_{\substack{\bar{c}\bar{c}\\ cc}}$ and $\rho_{\bar{g}g}$ being given by eq.(3.2.3) and considered to be constant and with $\rho_{\substack{\bar{e}\bar{e}\\ ee}} = \rho_{\bar{e}e} = \rho_{\bar{c}c} = 0$. A trick that further simplifies the calculation is to write each element as a sum of a magnetic-field-independent and a magnetic-field-dependent part, e.g. $\rho_{\bar{g}e} = \rho_{ge}^{(o)} + \rho_{ge}^{(B)}$, and recognize the fact that elements which are identical in the absence of the magnetic field shall now differ only in the sign of the magnetic-field-dependent part, e.g. $\rho_{g\bar{e}} = \rho_{ge}^{(o)} - \rho_{ge}^{(B)}$. Thus, by adding the equations for corresponding elements we solve for the magnetic-field-independent parts while by subtracting we solve for the magnetic-field-dependent parts, effectively breaking the solution of the 24 × 24 system in hand into two 12 × 12 systems. This procedure ultimately leads to the elements of interest:

$$\rho_{\substack{\bar{g}e\\ g\bar{e}}} = \rho_{ge}^{(o)} \pm \rho_{ge}^{(B)} \tag{3.2.6}$$

$$\begin{aligned}
\rho_{ge}^{(o)} &\simeq \frac{f_c(s)\frac{\Omega_d^2}{D_{pd}} - D_d^*\left[1 - \frac{R_{\mathtt{eff}}}{D_{pd}}\frac{f_g\ \ \Omega_d^2/D_{pd} + D_p R_{\mathtt{eff}}/D_{pd}}{D_p + \Omega_d^2/D_{pd}}\right]}{D_d^*\left[(D_p + \Omega_d^2/D_{pd}) - \frac{(D_p\frac{R_{\mathtt{eff}}}{D_{pd}})^2}{D_p + \Omega_d^2/D_{pd}}\right]}\, i\rho_{gg}^{(o)}\Omega_p \\
\rho_{ge}^{(B)} &\simeq \left[\frac{1 - 2\ \frac{R_{\mathtt{eff}}}{D_{pd}}\frac{1}{f_g}\frac{\Omega_d^2/D_{pd}}{D_p + \Omega_d^2/D_{pd}}}{D_p + \frac{\Omega_d^2}{D_{pd}}}\right]\ \frac{i\ \Omega_p\ {f_g}^2\rho_{gg}^{(o)}\ \Omega_L}{R_{\mathtt{eff}}}
\end{aligned} \tag{3.2.7}$$

where $D_p = R_{\mathtt{eff}} + \frac{\Gamma}{2} + i\delta_p$, $D_d = \frac{\Gamma}{2} + i\delta_d$ and $D_{pd} = R_{\mathtt{eff}} + \gamma_{gc} + i\delta_R$ (with $\delta_R = \delta_p - \delta_d$, the Raman detuning).

As expected, $\rho_{ge}^{(B)}$ is proportional to $\rho_{gg}^{(B)} \equiv {f_g}^2\frac{\Omega_L}{R_{\mathtt{eff}}}\rho_{gg}^{(o)}$, which is the magnetic field dependent part of the ground state populations, as can be seen from equation (3.2.3). Thus, the rotation angle, being dependent on $\Re(\rho_{\bar{g}e}) - \Re(\rho_{g\bar{e}}) = 2\ \Re(\rho_{ge}^{(B)})$, will ultimately be proportional to $P_x = \rho_{\bar{g}\bar{g}} - \rho_{gg} = 2\rho_{gg}^{(B)}$, as in the TLA case. Also it is useful to note that all equations, from (3.2.3) to (3.2.7), fall back to their TLA counterparts if one turns off the drive field, although an anticipated renormalization of the ground state populations to unity is required, to account for the non-zero populations of states $|c\rangle$ and $|\bar{c}\rangle$.

3.2.2 Sensitivity and Signal: Comparing to the TLA case

For the rotation angle, signal and sensitivity of the EIT magnetometer, the general equations (1.2.36), (1.2.2) [with α given by (1.2.37)] and (1.2.28) hold. However, to facilitate the comparison to the TLA case, we will relate corresponding quantities between the two cases by introducing *enhancement factors.* For example, the rotation angle in the EIT case is written as:

$$\phi_{\mathtt{EIT}} = \beta_\phi \ \phi_{\mathtt{TLA}} \tag{3.2.8}$$

where β_ϕ is the *Faraday rotation angle enhancement factor.* Also, the signal of the magnetometer takes the form:

$$S_{\mathtt{EIT}} = \beta_\alpha \ \beta_\phi \ S_{\mathtt{TLA}} \equiv \beta \ S_{\mathtt{TLA}} \tag{3.2.9}$$

where $\beta_\alpha = \frac{\exp(-\alpha_{\mathtt{EIT}} \ l)}{\exp(-\alpha_{\mathtt{TLA}} \ l)} \simeq \exp(\alpha_{\mathtt{TLA}} \ l)$ is the *transmitted intensity enhancement factor.* We note that β_α is expected to be a small quantity on the order of unity, due to the large detuning of the probe in the TLA magnetometer.

Regarding the noise in the signal, the various terms contributing to it have to be examined separately. First of all, spin projection noise, which is proportional to ΔJ_x, will be enhanced by β_ϕ, that is $\delta\phi^{(\mathtt{EIT})}_{\mathtt{spn}} = \beta_\phi \delta\phi^{(\mathtt{TLA})}_{\mathtt{spn}}$. The same will apply for the thermal Johnson noise, since it is due to a real magnetic field, which can not be separated from the magnetic field under measurement. Thus $\delta\phi^{(\mathtt{EIT})}_{\mathtt{th}} = \beta_\phi \ \delta\phi^{(\mathtt{TLA})}_{\mathtt{th}}$. On the other hand, photon shot noise and other non-magnetic noise sources are not affected by the enhancement of the rotation angle. This discussion leads to the conclusion that, if Johnson noise dominates over other sources, the TLA and EIT noise in the rotation angle can be related through the simple expression:

$$\mathcal{N}_{\mathtt{EIT}} \simeq \beta_\phi \mathcal{N}_{\mathtt{TLA}} = \sqrt{\left(\beta_\phi \delta\phi^{(\mathtt{TLA})}_{\mathtt{th}}\right)^2 + \mathcal{O}\left(\delta\phi^2_{\mathtt{other}}\right)} \tag{3.2.10}$$

So, if thermal noise is dominant, then equations (3.2.9) and (3.2.10) lead to:

$$\left(\frac{S}{\mathcal{N}}\right)_{\texttt{EIT}} \simeq \beta_\alpha \left(\frac{S}{\mathcal{N}}\right)_{\texttt{TLA}} \tag{3.2.11}$$

and since $\beta_\alpha \simeq 1$, we gain almost nothing in terms of signal to noise.

We note here, however, that the sensitivity of the magnetometer is not affected, since taking into account Equation (1.2.27) and the discussion above, we arrive at:

$$\delta B_{\texttt{EIT}} = \sqrt{\delta B^2_{\texttt{spn}} + \left(\frac{1}{\beta_\phi\sqrt{\beta_\alpha}}\delta B^{(\texttt{TLA})}_{\texttt{psn}}\right)^2 + \delta B^2_{\texttt{th}} + \delta B^2_{\texttt{e}}} \tag{3.2.12}$$

where the reduction of the photon shot noise sensitivity term comes from $\eta \propto 1/\kappa \propto 1/\phi$ and also $\eta \propto \sqrt{\exp(\alpha l)}$, and so, setting $\omega_{c,\texttt{TLA}} \simeq \omega_{c,\texttt{EIT}}$ to simplify things, we get that $\delta B^{(\texttt{EIT})}_{\texttt{psn}} \simeq \frac{1}{\beta_\phi\sqrt{\beta_\alpha}}\delta B^{(\texttt{TLA})}_{\texttt{psn}}$. Now, since psn is normally quite smaller than the other terms, we conclude that the sensitivity remains - almost - unchanged:

$$\delta B_{\texttt{EIT}} \simeq \delta B_{\texttt{TLA}} \tag{3.2.13}$$

Increasing the bandwidth

We are now going to show that what we don't gain in S/N ratio we gain in magnetometer bandwidth. We begin by noting that all discussions so far regarding the signal and sensitivity of the magnetometer are valid for AC magnetic field frequencies $\omega \ll \omega_c$, as mentioned in the original derivation of §1.2.3. It is easy to see that for $\omega \gg \omega_c$ it is:

$$\phi|_{\omega\gg\omega_c} \simeq \frac{\omega_c}{\omega}\phi|_{\omega\ll\omega_c} \quad \texttt{and} \quad \left.\frac{\partial\langle\phi\rangle}{\partial B_y}\right|_{\omega\gg\omega_c} \simeq \frac{\omega_c}{\omega}\left.\frac{\partial\langle\phi\rangle}{\partial B_y}\right|_{\omega\ll\omega_c} \tag{3.2.14}$$

a fact that affects both the signal and the magnetic originated thermal noise:

$$S|_{\omega\gg\omega_c} \simeq \frac{\omega_c}{\omega}S|_{\omega\ll\omega_c} \quad \texttt{and} \quad \delta\phi_{\texttt{th}}|_{\omega\gg\omega_c} \simeq \frac{\omega_c}{\omega}\,\delta\phi_{\texttt{th}}|_{\omega\ll\omega_c} \tag{3.2.15}$$

while noise sources of non-magnetic origin are not affected. So, equations (3.2.9) and (3.2.10) are modified as follows:

$$S_{\mathtt{EIT}}|_{\omega\gg\omega_c} \simeq \frac{\omega_c}{\omega}\beta S_{\mathtt{TLA}}|_{\omega\ll\omega_c} \tag{3.2.16}$$

$$\mathcal{N}_{\mathtt{EIT}}|_{\omega\gg\omega_c} = \sqrt{\left(\frac{\omega_c}{\omega}\beta_\phi \delta\phi^{\mathtt{(TLA)}}_{\mathtt{th}}|_{\omega\ll\omega_c}\right)^2 + \mathcal{O}\left(\delta\phi^2_{\mathtt{other}}\right)} \simeq \frac{\omega_c}{\omega}\beta_\phi \mathcal{N}_{\mathtt{TLA}}|_{\omega\ll\omega_c} \tag{3.2.17}$$

where the index "`other`" stands for all other, non-magnetic noise sources and the low-frequency TLA magnetometer quantities, $S_{\mathtt{TLA}}|_{\omega\ll\omega_c}$ and $\delta\phi^{\mathtt{(TLA)}}_{\mathtt{th}}|_{\omega\ll\omega_c}$, are being used as reference.

From the equations above we see how the bandwidth is extended in the EIT magnetometer as opposed to the TLA case, since the former maintains the signal to noise ratio of the latter up to frequencies $\omega \sim \beta_\phi\omega_c$. For example, for a typical TLA magnetometer bandwidth $\omega_c \simeq 2\pi \times 20$ Hz, as reported in [11] for Potassium, and a factor $\beta_\phi \simeq 50$, it follows that the EIT magnetometer is easily operated up to frequencies $\omega = \beta_\phi\omega_c \simeq 2\pi \times 1$ kHz. Using heavier alkali atoms, like Cesium, the transverse relaxation rate and, thus, the bandwidth increase, although the sensitivity becomes worse. In this case, the effective bandwidth of the EIT magnetometer reaches the falloff frequencies of thermal noise (a few kHz) and the magnetometer approaches shot-noise limited operation.

3.2.3 Numerical results and Plots

In this section we plug in some numbers for the parameters in order to calculate the Faraday rotation angle enhancement factor, which, as we saw, defines the bandwidth increase for the EIT magnetometer. First of all we assume the excitation rates for the the two cases, $R^{\mathtt{(EIT)}}_{\mathtt{ex}} = 2 \times R^{\mathtt{(TLA)}}_{\mathtt{ex}} = 4 \times \frac{1}{T_2}$, and a common probe beam Rabi frequency, $\Omega_p = 3.3\times10^{-4}\Gamma$, small enough for the linear approximations to adequately describe the exact systems. As mentioned earlier, in the EIT case and for a specific

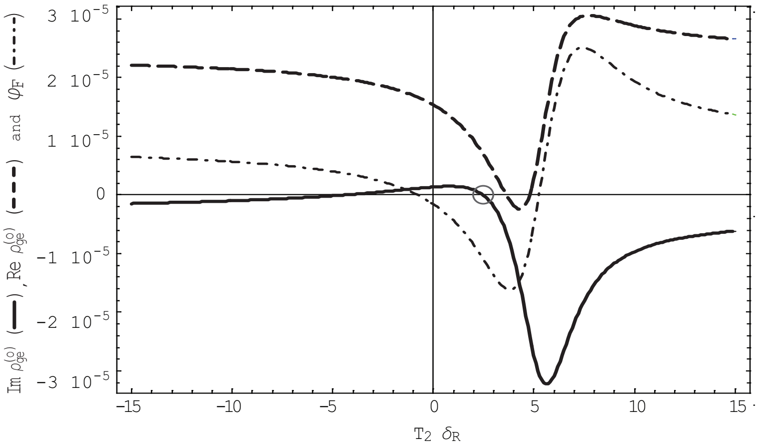

Figure 3.2: $\Im(\rho_{ge}^{(o)})$, $\Re(\rho_{ge}^{(o)})$ and ϕ_F (scaled down by a factor of 1000) vs δ_R at $T = 450^o$K. The circle points out the optimum operation point. Parameters: $R_{\texttt{ex}} = 4 \times \frac{1}{T_2} \simeq 2\pi \times 120\frac{\text{rad}}{\text{sec}}$, $\Omega_p = 3.3\ 10^{-4}\Gamma$, $\Omega_d = 0.011\ \Gamma$ and $\delta_d = 4\Gamma$

excitation rate, $R_{\texttt{ex}}$, we search for drive field detunings and Rabi frequencies such that zero absorption coincides with maximum rotation of the probe polarization. For example, it is found that for the aforementioned value of $R_{\texttt{ex}}$, an $\Omega_d \simeq 2\pi \times 0.7\sqrt{\frac{\Gamma}{T_2}}$ at $\delta_d = 4\Gamma$ provides the conditions for the probe to experience maximum rotation at zero absorption, at a probe detuning, δ_p, slightly larger than δ_d. We remind here, however, that the optimization of the EIT magnetometer, being a 3-parameter procedure, is achieved for various values of $R_{\texttt{ex}}$, Ω_d and δ_d. For this specific value of $R_{\texttt{ex}}$ there are many pairs of Ω_d and δ_d that optimize the conditions, and we pick the values above just to pick some. To illustrate the situation, we set the temperature at $T = 450^o$K, where $\frac{1}{T_2} \simeq 2\pi \times\ 30\frac{\text{rad}}{\text{sec}}$ and $\Omega_d \simeq 0.011\ \Gamma$, and in Figure 3.2 we depict the real and imaginary parts of $\rho_{ge}^{(o)}$ and the Faraday rotation angle near the Raman resonance. We see that there is an optimum detuning for the probe, $\delta_{p,\texttt{opt}}$, for which absorption is zero and rotation is maximum. Unfortunately no simple analytic expression has been found for the calculation of this $\delta_{p,\texttt{opt}}$ and for each temperature it is calculated numerically. On the contrary, the optimum TLA detuning is derived from equation (1.2.12) for $\Delta = \frac{\Gamma}{2}\sqrt{\frac{3n_d l\lambda^2}{8\pi}}$. So, in Figure 3.3 we plot the rotation angle enhancement factor, β_ϕ, for various temperatures, that is for various alkali vapor densities, which is the main result of this Chapter.

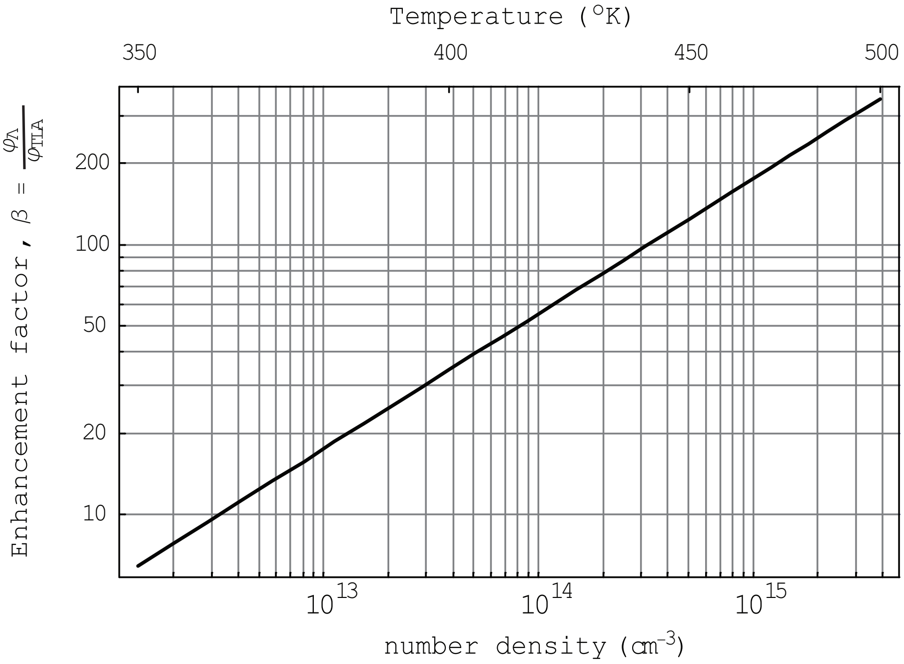

Figure 3.3: Faraday rotation angle enhancement factor, $\beta_\phi = \frac{\phi_{\mathrm{EIT}}}{\phi_{\mathrm{TLA}}}$

Chapter 4

Towards a more realistic model

In this chapter we introduce the full ^{85}Rb level structure and compare the actual Pump-Probe magnetometer and its EIT enhanced version to the corresponding toy-models we previously studied. Our aim is on one hand to establish the applicability of the idea in a realistic atomic system and on the other hand to show that the toy-model of the previous chapters gives an adequate qualitative description of the phenomena involved.

4.1 The level structure of ^{85}Rb

The transition of interest for the pump-probe magnetometer is the $5S_{1/2} \rightarrow 5P_{1/2}$ at 795nm, which is traditionally called the D1 line of Rb. The nucleus of ^{85}Rb has a nuclear spin $I = \frac{5}{2}$, so each of the $5S_{1/2}$ and $5P_{1/2}$ energy levels splits into an $F = 2$ and an $F = 3$ component, which in turn split into $2F + 1$ magnetic sub-levels with magnetic quantum numbers $|M_F| \leq F$. For the ground state ($5S_{1/2}$), the hyperfine splitting is $\Delta\omega^{(S)}_{\mathtt{hfs}} = 3.036$GHz and for the excited ($5P_{1/2}$) it is $\Delta\omega^{(P)}_{\mathtt{hfs}} = 362.1$MHz. A schematic drawing of this structure is given in the next section where the pump-probe magnetometer is described.

notation conventions

We use Latin characters for the hyperfine substates of the ground state ($5S_{1/2}$) and Greek characters for the excited state ($5P_{1/2}$). The actual characters used are given in the table below.

M_F	-3	-2	-1	0	1	2	3
$F=3$	q	w	e	o	r	t	y
$F=2$		s	d	c	f	g	
$F'=3$	μ	ς	ϵ	o	ρ	τ	υ
$F'=2$		σ	δ	ψ	ϕ	γ	

When indexing, we use the symbolic convention $i \in \{F = 2 \texttt{ or } 3\}$ if state $|i\rangle$ belongs to the $F = 2$ `or` $F = 3$ hyperfine manifold of the $5S_{1/2}$ and $i \in \{F' = 2 \texttt{ or } 3\}$ if state $|i\rangle$ belongs to the $F = 2$ `or` $F = 3$ hyperfine manifold of the $5P_{1/2}$.

Dipole transition matrix elements

The relative strength of a given $|F, M_F\rangle \longrightarrow |F', M'_F\rangle$ transition is determined by its dipole transition matrix element, which is expressed in terms of the reduced matrix element and the appropriate Clebsch-Gordan coefficient via the Wigner-Eckart theorem as [14]:

$$\langle F, M_F|D_q|F', M'_F\rangle = \sqrt{3}(-1)^{F-M_F}(F||D||F')\begin{pmatrix} F & 1 & F' \\ -M_F & q & M'_F \end{pmatrix} \tag{4.1.1}$$

where D is the electric dipole operator, q denotes the light polarization ($q = 0, \pm 1$ for π and $\sigma^{\mp}$ excitation, respectively) and $(F||D||F')$ is the, so called, *reduced matrix element*, which does not depend on the magnetic quantum numbers and is a tabulated quantity in textbooks of atomic data. The factor $\sqrt{3}$ is explained in the next section. The parenthesized structure in the right hand side of the above equation is called a *Wigner 3-J symbol* and is related to Clebsch-Gordan coefficients via:

$$C^{j_1\ j_2\ j}_{m_1 m_2 m} = (-1)^{-j_1+j_2-m}\sqrt{2j+1}\begin{pmatrix} j_1 & j_2 & j \\ m_1 & m_2 & -m \end{pmatrix} \tag{4.1.2}$$

If one defines the Rabi frequency of a coherent field through the reduced matrix element as $\Omega = \frac{(F||D||F')E}{2\hbar}$, then any given transition $|F, M_F\rangle \rightarrow |F', M'_F\rangle$ will be driven by a fraction of this Rabi frequency determined by the appropriate 3-J symbol. Finally, incoherent pumping and decay rates depend on the square of the dipole transition matrix element and, so, on the square of the 3-J symbols.

4.2 Pump-Probe magnetometer

The pump-probe magnetometer is the realistic version of the TLA magnetometer of the previous Chapters. We will study this first and then compare it to the EIT-enhanced version we propose.

In the pump-probe magnetometer, a broadband, incoherent, σ^+ polarized pump beam, pumps both the $F = 2$ and $F = 3$ ground states of the Rb vapor along the $\hat{\boldsymbol{z}}$-axis, transferring most of the population to the $|F = 3, M_F = 3\rangle$ ground state, thus creating a large $\hat{\boldsymbol{z}}$ polarization, P_z. The magnetic field along $\hat{\boldsymbol{y}}$-axis slightly rotates this polarization creating a small component along $\hat{\boldsymbol{x}}$-axis, which is detected by the Faraday rotation of a weak, narrowband, linearly polarized probe beam, propagating along $\hat{\boldsymbol{x}}$-axis and acting on the transitions $F = 3 \rightarrow F' = 2, 3$. We study this system by solving the Liouville equation along $\hat{\boldsymbol{z}}$-axis, which is the propagation axis of the *pump* beam, by appropriately rotating the Hamiltonians of both the probe and the magnetic field. Then we rotate the steady state density matrix back to the $\hat{\boldsymbol{x}}$-axis, since this is what we are interested in.

In the following we give plots and define the appropriate matrices for the various interactions.

4.2.1 natural decay

In Figure 4.1 we give the relative decay strengths for the various possible decay channels. For the sake of clarity (!?), the Figure is split into four segments one for each of the $F' = 2, 3 \to F = 2, 3$ possible initial-final hyperfine multiplets. We assume that each of the 12 $|F', M'_F\rangle$ excited states decays with a rate Γ, so the factor $\sqrt{3}$ appearing in equation (4.1.1) is necessary to ensure that:

$$\sum_{F',F,M'_F,M_F,q} \begin{pmatrix} F & 1 & F' \\ -M_F & q & M'_F \end{pmatrix}^2 = \sum_{F'=2}^{3} (2F'+1) = 12 \tag{4.2.1}$$

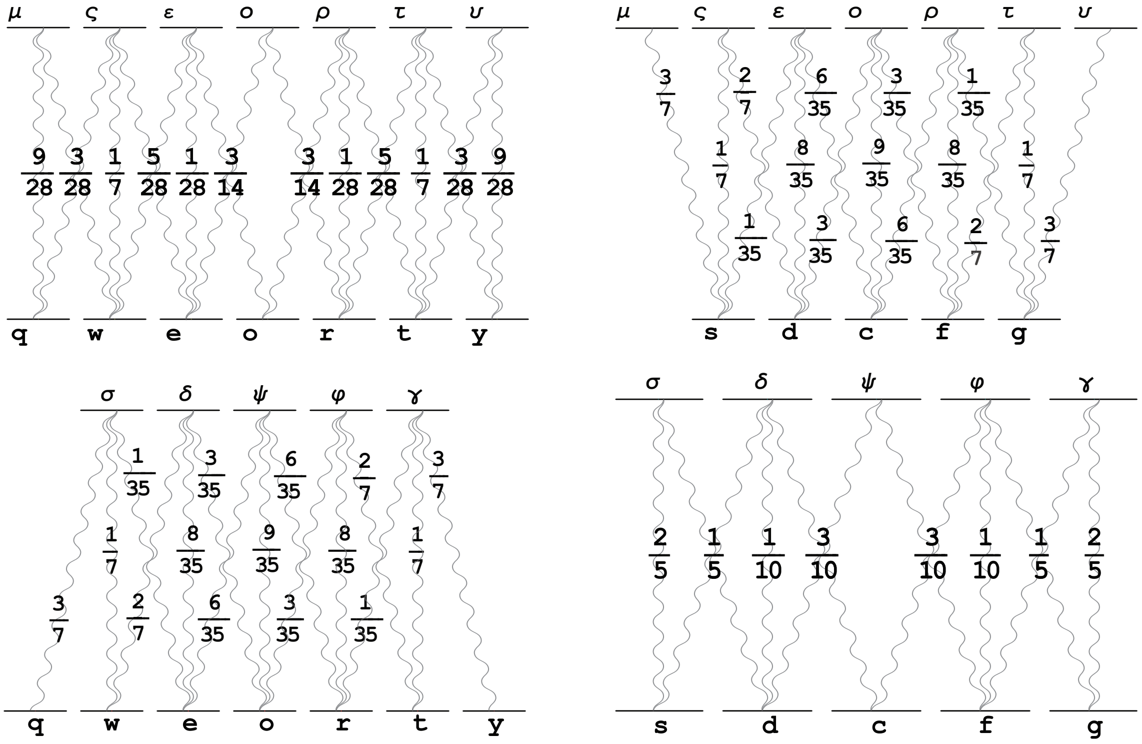

Figure 4.1: Natural decay relative strengths.
. top left: $F' = 3 \to F = 3$, top right: $F' = 3 \to F = 2$
. bottom left: $F' = 2 \to F = 3$, bottom right: $F' = 2 \to F = 2$

The relaxation matrix for the natural decay is defined by the following relations:

$$\begin{array}{rcl} \mathcal{R}^{(\mathtt{N})}_{\kappa\kappa} & = & -\Gamma\rho_{\kappa\kappa}, \quad \kappa \in \{F'=2,3\} \\ \mathcal{R}^{(\mathtt{N})}_{kk} & = & \Gamma \sum_{\kappa} \sum_{F_\kappa, M_\kappa, q} \begin{pmatrix} F_k & 1 & F_\kappa \\ -M_k & q & M_\kappa \end{pmatrix}^2 \rho_{\kappa\kappa}, \quad \begin{array}{rcl} k & \in & \{F=2,3\} \\ \kappa & \in & \{F'=2,3\} \end{array} \\ \mathcal{R}^{(\mathtt{N})}_{k\neq\kappa} & = & -\dfrac{\Gamma}{2}\rho_{k\kappa}, \quad \begin{array}{rcl} k & \in & \{F,F'=2,3\} \\ \kappa & \in & \{F'=2,3\} \end{array} \\ \mathcal{R}^{(\mathtt{N})}_{k\neq l} & = & 0, \quad k,\ l \in \{F=2,3\} \end{array} \qquad (4.2.2)$$

The first and second relations describe decay of the excited and increase of the ground populations, respectively, while the third and fourth describe the decoherence of the off-diagonal density matrix elements.

4.2.2 Optical Pumping

The optical pumping procedure, as seen along $\hat{\boldsymbol{z}}$-axis is depicted in Figure 4.2. The corresponding pumping matrix is defined by:

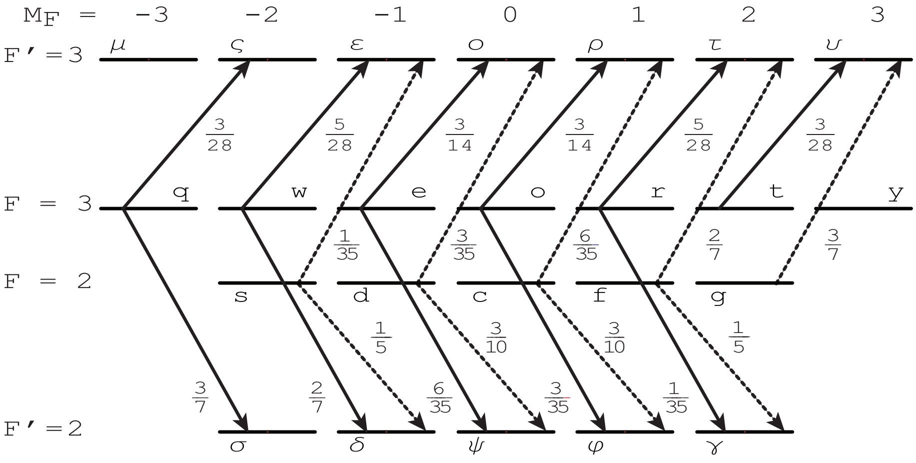

Figure 4.2: Pump-probe magnetometer optical pumping relative strengths ($\hat{\boldsymbol{z}}$-axis).
. solid: $F = 3 \rightarrow F' = 2,3$, dotted: $F = 2 \rightarrow F' = 2,3$.
. For clarity, the excited $F' = 2$ hyperfine multiplet is drawn at the bottom.

$$
\begin{aligned}
\mathcal{R}^{\texttt{(P,TLA)}}_{kk} &= -R_{\texttt{ex}} \sum_{F_\kappa, M_\kappa} \begin{pmatrix} F_k & 1 & F_\kappa \\ -M_k & -1 & M_\kappa \end{pmatrix}^2 \rho_{kk}, \quad k \in \{F = 2,3\} \\
\mathcal{R}^{\texttt{(P,TLA)}}_{\kappa\kappa} &= R_{\texttt{ex}} \sum_{F_k, M_k} \begin{pmatrix} F_k & 1 & F_\kappa \\ -M_k & -1 & M_\kappa \end{pmatrix}^2 \rho_{kk}, \quad \begin{array}{rcl} k & \in & \{F = 2,3\} \\ \kappa & \in & \{F' = 2,3\} \end{array} \\
\mathcal{R}^{\texttt{(P,TLA)}}_{k\neq\kappa} &= \frac{\mathcal{R}(\rho)^{\texttt{(P)}}_{kk}}{2\rho_{kk}} \rho_{k\kappa}, \quad \begin{array}{rcl} k & \in & \{F = 2,3\} \\ \kappa & \in & \{F, F' = 2,3\} \end{array} \\
\mathcal{R}^{\texttt{(P,TLA)}}_{\kappa\neq\lambda} &= 0, \quad \kappa, \lambda \in \{F' = 2,3\}
\end{aligned}
\tag{4.2.3}
$$

with $R_{\texttt{ex}}$ the excitation rate. Again the first and second relations describe pumping *from* the ground *to* the excited states, while the third and fourth describe the decoherence of the off-diagonal density matrix elements.

4.2.3 Probe interaction

The probe field acts on the $|F = 3, M_F\rangle \rightarrow |F' = 2,3, M'_F = M_F \pm 1\rangle$ transitions. The situation along its propagation axis, $\hat{\boldsymbol{x}}$, is shown in Figure 4.3. The Hamiltonian along the same axis is defined by:

$$
\begin{aligned}
\mathcal{H}^{\texttt{(pr)}}_{k\kappa} &= \hbar\Omega_p \left[\left| \begin{pmatrix} F_k & 1 & F_\kappa \\ -M_k & 1 & M_\kappa \end{pmatrix} \right| + \left| \begin{pmatrix} F_k & 1 & F_\kappa \\ -M_k & -1 & M_\kappa \end{pmatrix} \right| \right], \quad \begin{array}{rcl} k & \in & \{F = 3\} \\ \kappa & \in & \{F' = 2,3\} \end{array} \\
\mathcal{H}^{\texttt{(pr)}}_{k\kappa} &= 0, \quad k \in \{F = 2\} \\
\mathcal{H}^{\texttt{(pr)}}_{kk} &= \hbar\delta, \quad k \in \{F = 3\} \\
\mathcal{H}^{\texttt{(pr)}}_{kk} &= 0, \quad k \in \{F = 2\} \\
\mathcal{H}^{\texttt{(pr)}}_{\kappa\kappa} &= 0, \quad \kappa \in \{F' = 3\} \\
\mathcal{H}^{\texttt{(pr)}}_{\kappa\kappa} &= 10.5\ \hbar\Gamma, \quad \kappa \in \{F' = 2\}
\end{aligned}
\tag{4.2.4}
$$

where Ω_p is the probe beam Rabi frequency, δ its detuning with reference to the $F = 3 \rightarrow F' = 3$ transition and the term $10.5\ \Gamma \simeq 362.1$MHz in the last equation is

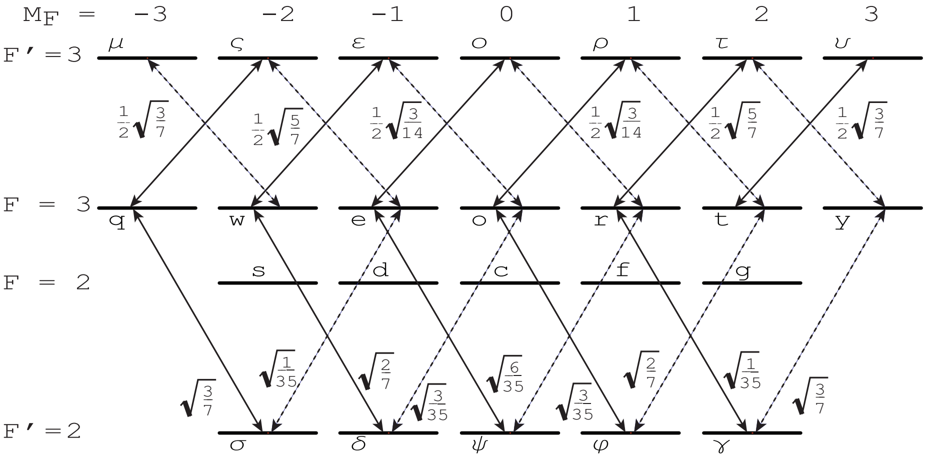

Figure 4.3: Probe transitions relative strengths ($\hat{\boldsymbol{x}}$-axis). solid: σ^+, dotted: σ^-

the extra detuning for the $F = 3 \rightarrow F' = 2$ transition, due to the hyperfine splitting of the $5P_{1/2}$ state. For the solution of the Liouville equation the above Hamiltonian is rotated by $\pi/2$ about $\hat{\boldsymbol{y}}$-axis with the help of the appropriate rotation matrix defined in Appendix B:

$$\mathcal{H}_z^{(\mathtt{pr})} = U_y(\pi/2) \cdot \mathcal{H}^{(\mathtt{pr})} \cdot U_y^{\dagger}(\pi/2) \qquad (4.2.5)$$

4.2.4 Magnetic interaction

The magnetic field lies along the $\hat{\boldsymbol{y}}$-axis and its Hamiltonian can be defined by:

$$\begin{aligned} \mathcal{H}_{kk}^{(\mathtt{B})} &= M_k \hbar \Omega_L, \quad k \in \{F, F' = 2, 3\} \\ \mathcal{H}_{k \neq l}^{(\mathtt{B})} &= 0, \quad k, l \in \{F, F' = 2, 3\} \end{aligned} \qquad (4.2.6)$$

When written like this, this Hamiltonian assumes $\hat{\boldsymbol{y}}$ to be the quantization axis. To rotate it along what we consider to be the quantization axis in our problem, that is the propagation axis of the pump beam, $\hat{\boldsymbol{z}}$, we have to perform a y-type rotation through

$\pi/2$ followed by a z-type rotation through $\pi/2$. So the magnetic field Hamiltonian we use in our calculations is:

$$\mathcal{H}_z^{(\mathtt{B})} = U_z(\pi/2) \cdot U_y(\pi/2) \cdot \mathcal{H}^{(\mathtt{B})} \cdot U_y^{\dagger}(\pi/2) \cdot U_z^{\dagger}(\pi/2) \tag{4.2.7}$$

4.2.5 Spin decoherence

Decoherence of the spins due to spin exchange and spin destruction collisions is the last relaxation process that has to be taken into account. We only allow coherences between nearest neighbors (pairs of states with $\Delta F = 0, \pm 1$ and $\Delta M = 0, \pm 1$) to be non-zero and assume they decay with a rate $1/T_2$. So the spin relaxation matrix will be defined by:

$$\begin{aligned}
\mathcal{R}_{kl}^{(T_2)} &= -(\delta_{M_k,M_{l+1}} + \delta_{M_k,M_{l-1}})\frac{1}{T_2}\rho_{kl}, & \begin{array}{rcl} k,l &\in& \{F(F')=2\} \text{ or} \\ k,l &\in& \{F(F')=3\} \end{array} \\
\mathcal{R}_{kl}^{(T_2)} &= -(\delta_{M_k,M_{l+1}} + \delta_{M_k,M_l} + \delta_{M_k,M_{l-1}})\frac{1}{T_2}\rho_{kl}, & \begin{array}{rcl} k &\in& \{F(F')=2\} \text{ and} \\ l &\in& \{F(F')=3\} \end{array} \\
\mathcal{R}_{kl}^{(T_2)} &= 0, \quad \text{for all other elements}
\end{aligned} \tag{4.2.8}$$

4.2.6 Steady state solution

The Liouville equation, expressed along the propagation direction of the pump beam, $\hat{\boldsymbol{z}}$, is given by:

$$\dot{\rho_z} = -\frac{i}{\hbar}\left[\left(\mathcal{H}_z^{(\mathtt{pr})} + \mathcal{H}_z^{(\mathtt{B})}\right), \rho_z\right] + \left(\mathcal{R}^{(\mathtt{N})} + \mathcal{R}^{(\mathtt{P,TLA})} + \mathcal{R}^{(T_2)}\right) \tag{4.2.9}$$

and is solved numerically for the steady state. The resulting steady state density matrix, $\rho_z^{\mathtt{ss}}$, is rotated around $\hat{\boldsymbol{y}}$ through $-\pi/2$ to give the desired result, which is the steady state density matrix along $\hat{\boldsymbol{x}}$-axis:

$$\rho^{\mathtt{ss}} = U_y^{\dagger}(\pi/2) \cdot \rho_z^{\mathtt{ss}} \cdot U_y(\pi/2) \tag{4.2.10}$$

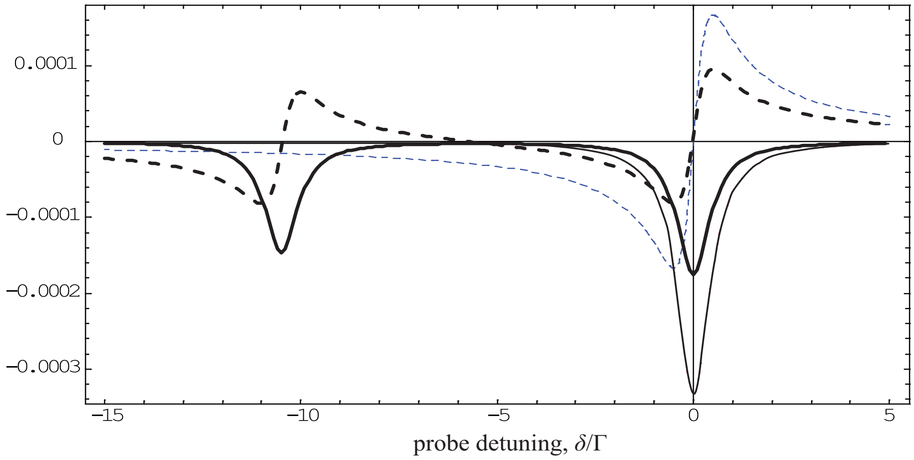

Figure 4.4: Absorption (solid) and dispersion (dashed) of the probe beam (thick: full system / thin: toy TLA system). Parameters: $\Omega_p = 0.00033\Gamma$

The quantities of interest are the absorption of the probe, related to the sum of the imaginary parts of all $|F=3, M_F\rangle \rightarrow |F'=2,3, M'_F = M_F \pm 1\rangle$ density matrix elements, and the Faraday rotation angle of the polarization plane of the probe, related to the the difference of the real parts of the $|F=3, M_F\rangle \rightarrow |F'=2,3, M'_F = M_F+1\rangle$ and $|F=3, M_F\rangle \rightarrow |F'=2,3, M'_F = M_F-1\rangle$ elements. So, if I_o and $I_{\texttt{tr}}$ are the incident and transmitted intensities of the probe beam, they will be connected through:

$$I_{\texttt{tr}} = I_o \exp\left[-\frac{3n_d\lambda_o^2 l}{8\pi\tilde{\Omega}_p}\,\frac{1}{2}\sum_{\substack{k\in\{F=3\}\\ \kappa\in\{F'=2,3\}}}(\delta_{M_k,M_{\kappa-1}}+\delta_{M_k,M_{\kappa+1}})\Im(\rho_{k\kappa})\right] \tag{4.2.11}$$

while the rotation angle will be:

$$\phi_F = \frac{3n_d\lambda_o^2 l}{8\pi\tilde{\Omega}_p}\sum_{\substack{k\in\{F=3\}\\ \kappa\in\{F'=2,3\}}}(\delta_{M_k,M_{\kappa-1}}-\delta_{M_k,M_{\kappa+1}})\Re(\rho_{k\kappa}) \tag{4.2.12}$$

We remind that $\tilde{\Omega}_p = \Omega_p/\Gamma$ is the normalized Rabi frequency. Typical absorption and dispersion curves for the full system are shown along with their toy TLA model counterparts in Figure 4.4. As in the simple toy model, for detunings $\delta \gg \Gamma$, dispersion scales as $1/\delta$ and absorption as $1/\delta^2$.

4.2.7 Pump-probe magnetometer signal

The signal of the magnetometer is given by equation (1.2.2), $S = 2\phi_F I_{\mathtt{tr}}$, and for a specific temperature its dependence on the detuning of the probe beam has the typical form shown in Figure 4.5(a). By maximizing the signal we determine the optimum operation detuning and, consequently, the optimum Faraday rotation angle, which is plotted versus the atomic number density and the temperature in Figure 4.5(b), along with the corresponding plot for the toy TLA model studied in Chapter 1. The discrepancy between the two plots is due to leakage of population to the $F = 2$ ground state of the full system and the weakening of dispersion due to the extra 362.1MHz detuning of the $|F = 3\rangle \rightarrow |F' = 2\rangle$ transition. The value used for the excitation rate, $R_{\mathtt{ex}} = 32/T_2$, is the one maximizing the optimum Faraday rotation angle.

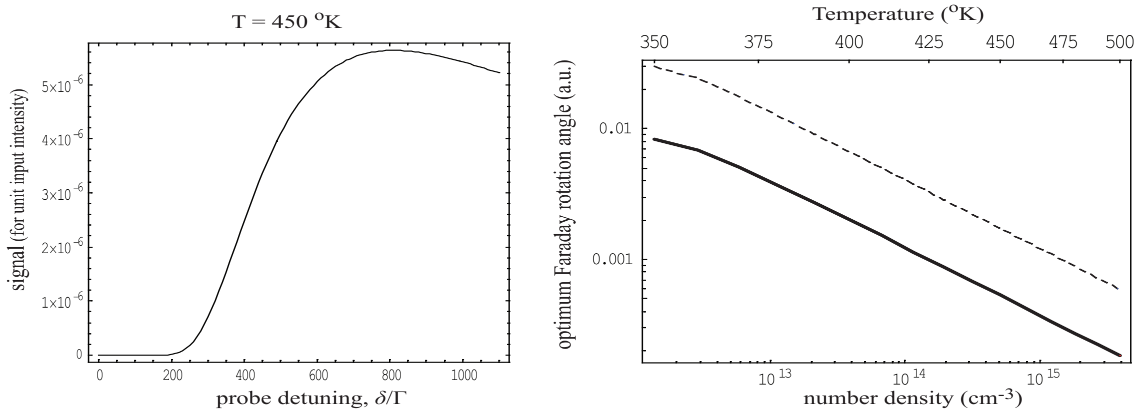

(a)

(b)

Figure 4.5: (a) Plot of signal vs detuning ($T = 450^o$K, $B = 1$fT, $R_{\mathtt{ex}} = 32/T_2$)
. (b) Optimum ϕ_F vs n_d (dashed: toy TLA model / solid: full model)

4.3 EIT enhanced Pump-Probe magnetometer

In order to create EIT conditions for the probe field, we introduce the drive field, which acts on the transitions $|F = 2, M_F\rangle \rightarrow |F' = 2, 3, M'_F = M_F \pm 1\rangle$. Also, optical pumping is now performed only on the $F = 3$ ground hyperfine multiplet. The drive field transitions along the propagation direction of the drive ($\hat{\boldsymbol{x}}$) and the optical pumping along $\hat{\boldsymbol{z}}$ are depicted in Figures 4.6 and 4.7, respectively.

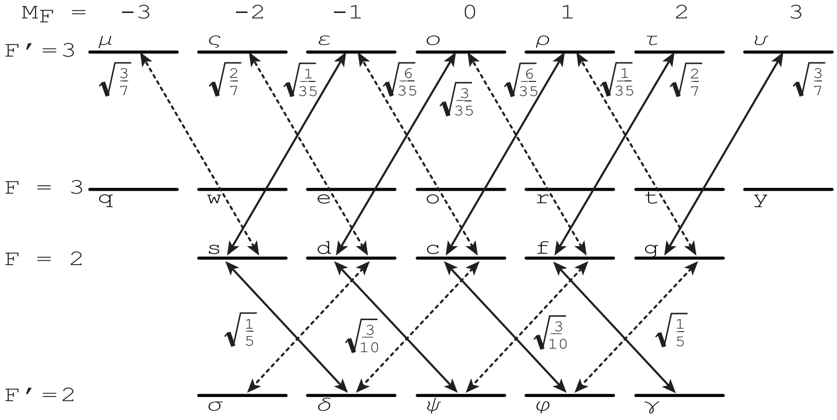

Figure 4.6: Drive transitions relative strengths ($\hat{\boldsymbol{x}}$-axis). solid: σ^+, dotted: σ^-

The Hamiltonian for the drive field interactions will be defined by:

$$\begin{aligned}
\mathcal{H}^{(\mathtt{dr})}_{k\kappa} &= \hbar\Omega_d \left[\left| \begin{pmatrix} F_k & 1 & F_\kappa \\ -M_k & 1 & M_\kappa \end{pmatrix} \right| + \left| \begin{pmatrix} F_k & 1 & F_\kappa \\ -M_k & -1 & M_\kappa \end{pmatrix} \right| \right], \quad \begin{matrix} k & \in & \{F = 2\} \\ \kappa & \in & \{F' = 2, 3\} \end{matrix} \\
\mathcal{H}^{(\mathtt{dr})}_{kk} &= \hbar\delta_d, \quad k \in \{F = 2\} \\
\mathcal{H}^{(\mathtt{dr})}_{kk} &= 0, \quad \text{for all other elements} \qquad (4.3.1)
\end{aligned}$$

and the optical pumping matrix by:

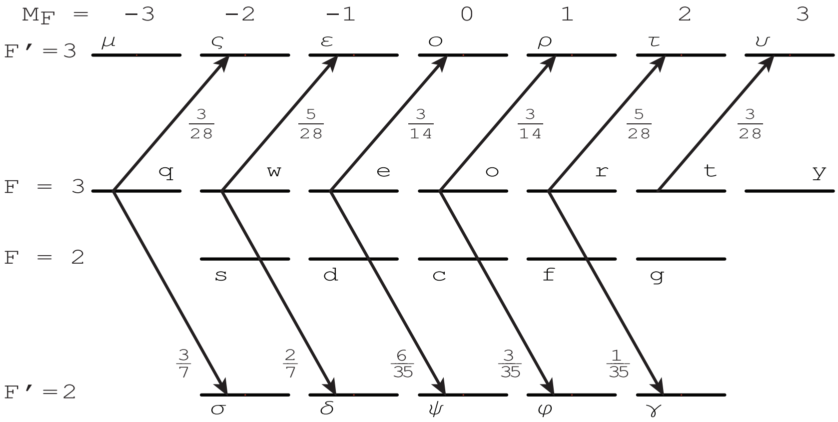

Figure 4.7: EIT OP magnetometer optical pumping relative strengths ($\hat{\boldsymbol{z}}$-axis).
. For clarity, the excited $F' = 2$ hyperfine multiplet is drawn at the bottom.

$$
\begin{aligned}
\mathcal{R}^{\texttt{(P,EIT)}}_{kk} &= -R\sum_{F_\kappa, M_\kappa}\begin{pmatrix} F_k & 1 & F_\kappa \\ -M_k & -1 & M_\kappa \end{pmatrix}^2 \rho_{kk}, \quad k \in \{F=3\} \\
\mathcal{R}^{\texttt{(P,EIT)}}_{\kappa\kappa} &= R\sum_{F_k, M_k}\begin{pmatrix} F_k & 1 & F_\kappa \\ -M_k & -1 & M_\kappa \end{pmatrix}^2 \rho_{kk}, \quad \begin{matrix} k & \in & \{F=3\} \\ \kappa & \in & \{F'=2,3\} \end{matrix} \\
\mathcal{R}^{\texttt{(P,EIT)}}_{k\neq\kappa} &= \frac{\mathcal{R}(\rho)^{\texttt{(P)}}_{kk}}{2\rho_{kk}}\rho_{k\kappa}, \quad \begin{matrix} k & \in & \{F=3\} \\ \kappa & \in & \{F, F'=2,3\} \end{matrix} \\
\mathcal{R}^{\texttt{(P,EIT)}}_{\kappa\neq\lambda} &= 0, \quad \kappa, \lambda \in \{F'=2,3\} \text{ or } \{F=2\}
\end{aligned}
\tag{4.3.2}
$$

The Liouville equation now takes the form:

$$
\dot{\rho_z} = -\frac{i}{\hbar}\left[\left(\mathcal{H}^{\texttt{(pr)}}_z + \mathcal{H}^{\texttt{(dr)}}_z + \mathcal{H}^{\texttt{(B)}}_z\right), \rho_z\right] + \left(\mathcal{R}^{\texttt{(N)}} + \mathcal{R}^{\texttt{(P,EIT)}} + \mathcal{R}^{(T_2)}\right) \tag{4.3.3}
$$

and is again solved along the $\hat{\boldsymbol{z}}$-axis and the resulting steady state density matrix is rotated along $\hat{\boldsymbol{x}}$. A typical absorption-dispersion profile near the Raman resonance is shown in Figure 4.8(a), while in Figure 4.8(b) the rotation angle profile is plotted. In these plots, the optimum operation detuning is pointed out with a small circle. It is seen from this plot that, while the full system is more rich in features, the simple toy-model adopted in the previous chapter gives an adequate qualitative description of the medium response.

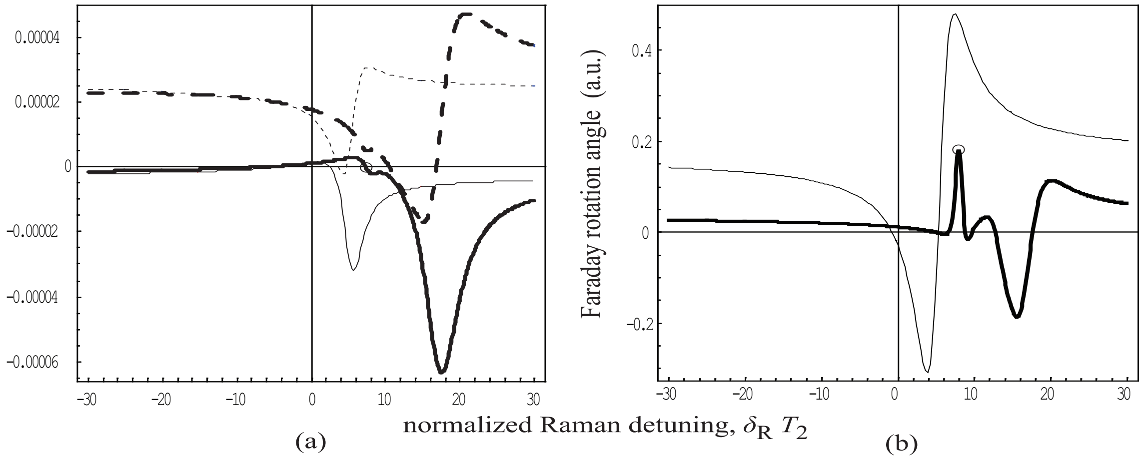

Figure 4.8: (a) Absorption (solid) and dispersion (dashed) of the probe beam. (b) Faraday rotation angle (thick lines: full system / thin lines: toy EIT system) Parameters: $T = 450^o$K, $\delta_d = 4\Gamma$, $\Omega_p = 0.00033\Gamma$ and $R_{\mathtt{ex}} = 4/T_2$, $\Omega_d = 0.011\Gamma$ for the toy EIT system and $R_{\mathtt{ex}} = 16/T_2$, $\Omega_d = 0.023\Gamma$ for the full system

4.3.1 Comparison to the Pump-Probe magnetometer

In Figure 4.9(a) we compare the optimum Faraday rotation angles for the TLA based and EIT enhanced magnetometers, both in the simple toy-model case as well as in the full system approach and in (b) the Faraday rotation angle enhancement factors are depicted. We observe that, while the Faraday rotation angles expected from the full systems are smaller than those calculated for the toy-models, the enhancement factor is the same in both cases and one can say, once more, that the simple models of the previous chapters give an adequate understanding of the works of the EIT enhanced magnetometer.

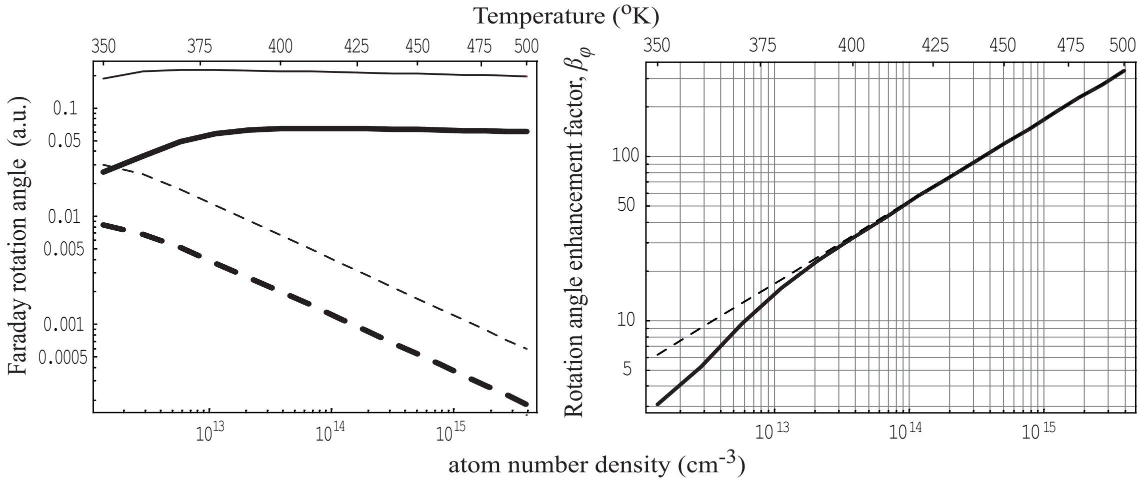

(a) (b)

Figure 4.9: (a) ϕ_F vs n_d [dashed: TLA based / solid: EIT enhanced].
. (b) β_F vs n_d [thick: full system / thin: toy model]

4.4 Inclusion of Doppler broadening

Having concluded that the toy models of the previous chapters give an acceptable qualitative description of the pump-probe magnetometer and its EIT enhanced version, we are now going to use the analytical expressions for the various quantities of interest obtained for these models in order to study the impact of Doppler broadening on the operation of the magnetometers.

Doppler broadening origins

In experiments where the speed of the atoms is either very small (e.g. in a BEC or a MOT) or uniform (e.g. in an atomic beam), the Doppler broadening of the spectral lines can be ignored. If, however, an experiment is to be performed using thermal atoms confined in a vapor cell, then the Doppler effect has to be taken into account.

If one considers a Maxwell distribution for the velocities of the atoms, Doppler broadening is introduced by integrating the density matrix elements over this distribution. If n_d is the atom number density, m the mass of an atom and $\upsilon_{\texttt{rms}} = \sqrt{\frac{k_B T}{m}}$ the root mean square atomic velocity, then the one dimensional Maxwell distribution (along $\hat{\boldsymbol{x}}$, which is assumed to be the axis of propagation of the beams) is expressed as [12]:

$$P(\upsilon_x)d\upsilon_x = \frac{d\upsilon_x}{\upsilon_{\texttt{rms}}\sqrt{2\pi}}\, e^{-\frac{1}{2}\upsilon_x^2/\upsilon_{\texttt{rms}}^2} \tag{4.4.1}$$

where υ_x is the atomic velocity projection along $\hat{\boldsymbol{x}}$. Thus the Doppler broadened matrix element ρ_{ij} will be a convolution of the Gaussian Maxwell distribution and the normal ρ_{ij} form:

$$\rho_{ij} = \frac{1}{\upsilon_{\texttt{rms}}\sqrt{2\pi}} \int_{-\infty}^{\infty} \rho_{ij}(\upsilon_x) e^{-\frac{1}{2}\upsilon_x^2/\upsilon_{\texttt{rms}}^2} d\upsilon_x \tag{4.4.2}$$

where the dependence of ρ_{ij} on υ comes from the fact that the detunings of the fields, due to the Doppler effect, will have to be replaced by:

$$\Delta_p = \delta_p - k_p \upsilon_x \;\; \texttt{and} \;\; \Delta_d = \delta_d - k_d \upsilon_x \tag{4.4.3}$$

with $k_{p\ (d)} = \frac{2\pi}{\lambda_{p\ (d)}}$ being the wavevector of the probe (drive) beam. The impact of the Doppler effect on the observable quantities of a transition is characterized by the quantity $k\upsilon_{\texttt{rms}}$: for atoms of a certain temperature, the smaller the wavelength (the larger the frequency), the larger the Doppler broadening of the transition and vice versa. For a certain transition, the larger the temperature, the larger the Doppler broadening.

Equation (4.4.2) does not generally yield analytic results, although when the Doppler width is either very wide or very narrow compared to the homogenous width ($k\upsilon_{\texttt{rms}} \gg \gamma_{ij}$ or $k\upsilon_{\texttt{rms}} \ll \gamma_{ij}$) then the Maxwell function can be pulled out of the integral or be replaced by a δ-function, respectively. However, when Doppler and homogenous broadening are comparable ($k\upsilon_{\texttt{rms}} \simeq \gamma_{ij}$), equation (4.4.2) has to be evaluated as is.

Doppler effect and EIT

Regarding its effect on EIT, Doppler effect tends to broaden both components of the Autler-Townes doublet, thus narrowing the EIT feature between them to extinction. This is because EIT induced in one velocity group will act to cover that induced in other groups. Moreover, if the wavelengths of the probe and drive transitions are unequal, a situation which is very common, then fulfilment of the EIT conditions in one velocity group does not imply that EIT conditions are fulfilled in other groups. However, EIT can still be observed if the drive beam has high enough input power. Physically this happens because power broadening of the $|c\rangle \leftrightarrow |e\rangle$ transition forces more velocity groups to take part in the formation of EIT.

A side effect of Doppler broadening is that it *suggests* (if not *dictates*) the relative propagation direction of the two beams. Specifically, since $\Delta_p - \Delta_d$ must be zero to observe EIT in a Λ-system, it follows that the two beams should co-propagate. It turns out that the same holds for a V-system, while in a Ξ-system the beams should counter-propagate, since the EIT condition there is $\Delta_p + \Delta_d = 0$.

Doppler broadened absorption-dispersion profiles

The Doppler broadened absorption and dispersion profiles for the TLA and EIT cases come from the integration of equations (1.2.34) and (3.2.6) [via (3.2.7)], respectively, according to equation (4.4.2). An example of these profiles is shown in Figure 4.10. For the TLA case, notice that the unbroadened curves break out of the graph. This is due to the area under the absorption curves being the same in both cases. As a consequence, the unbroadened media absorbs much more strongly on resonance and much more weakly a few natural widths, Γ, away from it. In the EIT case we are interested in demonstrating the same features as in the atoms-at-rest case of the previous chapter, that is large rotation angles at detunings of negligible absorption. In Figure 4.10, on the right side, we see that a region of gain can still be found and one can tune the probe beam to a zero-absorption detuning. The drive field Rabi frequency used for the plot and mentioned in the legend is the one that gives the

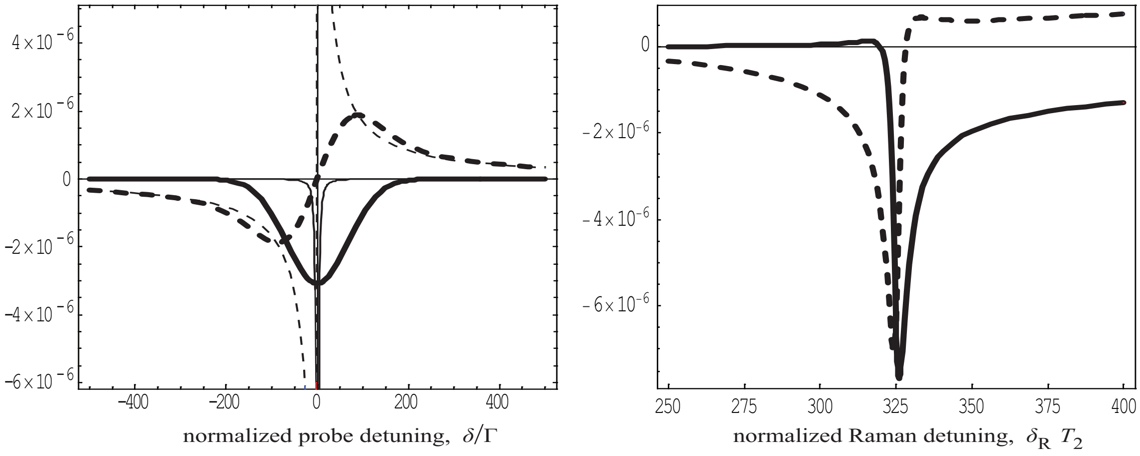

Figure 4.10: Absorption (solid) and dispersion (dashed) curves.
. Left: TLA case with $\Omega_p = 0.00033\Gamma$ and $R_{\texttt{ex}} = 2/T_2$.
. Thick lines: Doppler broadened media ($T = 450^o$K) / Thin: atoms at rest.
. Right: EIT case with $\delta_d = 200\Gamma$, $\Omega_p = 0.00033\Gamma$, $R_{\texttt{ex}} = 8/T_2$ and $\Omega_d = 0.6\Gamma$

maximum rotation angle for a $\sim$ 1fT magnetic field, for these particular values of δ_d, $R_{\texttt{ex}}$ and temperature. Comparing to the Doppler-free case, Fig. 3.2 or 4.8(a), we see that the gain region is obtained at much higher detunings and drive field Rabi frequencies. Large detunings are necessary because the lowering and broadening of the dispersion profile forces one to tune near the dispersion peak in order to achieve large rotation angles, while a large Ω_d is needed for the *penetration* of the Doppler profile and the creation of EIT, as explained in the previous paragraph. We note here that a drive field detuning, δ_d, on the order of 200Γ is still quite smaller than the hyperfine splitting of the $5\mathrm{S}_{1/2}$ ($\sim$ 600Γ). However, even after optimizing all parameters, the EIT scheme rotation angles are expected to be smaller than their Doppler-free counterparts, $\phi_{\texttt{EIT}}^{\texttt{(Doppler)}} < \phi_{\texttt{EIT}}^{\texttt{(Doppler-Free)}}$, due to the overall decrease of dispersion. On the other hand, the ordinary TLA-based magnetometer is not affected by Doppler broadening because it is usually operated at detunings quite larger than the Doppler width, thus $\phi_{\texttt{TLA}}^{\texttt{(Doppler)}} \simeq \phi_{\texttt{TLA}}^{\texttt{(Doppler-Free)}}$. As a consequence, the Faraday rotation enhancement factor, β_ϕ, is expected to decrease due to the Doppler effect.

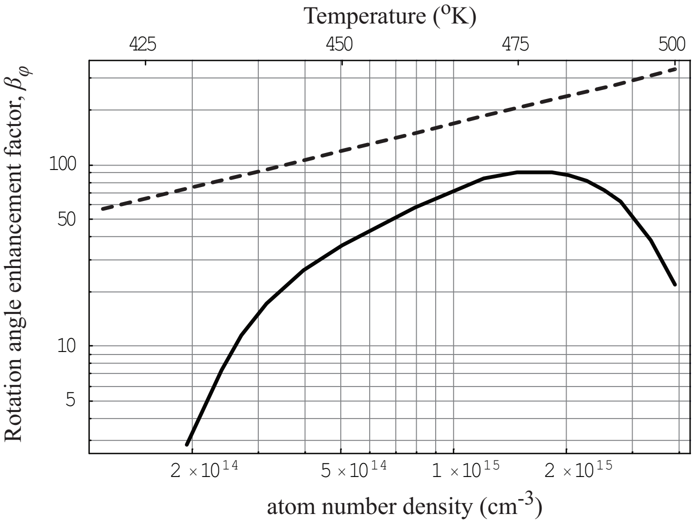

Figure 4.11: β_ϕ in the Doppler broadened case

This is evident in Figure 4.11 where β_ϕ is plotted versus the atomic number density for the Doppler-free (dashed) and Doppler-including (solid) cases. For the drawing of this plot, the drive field detuning was kept at $\delta_d = 200\Gamma$, while the values of Ω_d and $R_{\texttt{ex}}$ were optimized numerically for each value of the number density of atoms. In the same Figure, apart from the expected quantitative discrepancies between the two cases, we also see that Doppler effect affects the system qualitatively. For number densities below $\sim 2\times10^{14}$ cm^{-3}, no significant enhancement could be achieved. The reason for this is the large values of Ω_d needed for the creation of EIT conditions. For large Ω_d's and in order for a region of gain to appear, large excitation rates are required (on the order of $50\times\frac{1}{T_2}$ at $T\sim 420$°K or more for even lower temperatures). Such values of $R_{\texttt{ex}}$ diminish both the sensitivity of the magnetometer and the Faraday rotation angle due to the deterioration of the $\hat{\boldsymbol{x}}$-polarization, which is generally inversely proportional to R, and thus to $R_{\texttt{ex}}$, as seen in (1.2.7). However, for larger temperatures, the values of Ω_d required for EIT do not change significantly, since these depend on the Doppler width which increases as $\sqrt{T}$, whereas $\frac{1}{T_2}$ increases exponentially. As a consequence, a range of temperatures exists, where the relative values of $R_{\texttt{ex}}$ ($\sim$ a few $\frac{1}{T_2}$) and

Ω_d are suitable for the desirable operation of the magnetometer, with the system demonstrating large enhancement factors (peak value: $\beta_\phi \sim 90$ at $n_d \sim 1.5\times10^{15}$ cm^{-3} or $T \sim 475°$K) and excellent sensitivity. In conclusion, although Doppler effect seems to heavily deteriorate the operation of the proposed scheme, there appears to be a region of operating parameters which lead to the desired results.

Conclusion

Pump-Probe magnetometers are by now well established and documented. While they demonstrate excellent sensitivity in the quasi-static magnetic field regime, they have very limited bandwidth in the measurement of AC magnetic fields. We propose creating Electromagnetically Induced Transparency conditions for the probe laser beam of such a device, by use of a *drive* laser beam tuned to a different hyperfine transition of the atoms. By using a simple atom model consisting of spin-1/2 states, we conclude that the proposed scheme can in principle demonstrate a bandwidth increase on the order of 10^2, while maintaining excellent signal to noise ratio. The results are verified by numerically applying the same scheme on a realistic ^{85}Rb level structure. Finally, inclusion of the Doppler effect leads to substantially worse results for the most part, but a region of operating parameters which lead to highly increased bandwidth can still be obtained.

Future work on this subject involves including a buffer gas in the calculations, so that we can explore the potential of such a system as a magnetic imaging device. The ultimate goal is the study of a realistic alkali atom model, with all hyperfine states included, and with buffer gas, Doppler broadening and propagation effects taken into account and, of course, the experimental implementation of the device.

Appendix A

The transverse relaxation time, T_2

The transverse relaxation time, T_2, of an alkali vapor depends on spin-exchange (SE) and spin-destruction (SD) collisions and on diffusion of the alkali atoms out of the interaction volume. In the spin-exchange relaxation-free regime of high alkali densities [7], [6], diffusion and SD collisions are dominant and T_2 will be given by

$$\frac{1}{T_2} = \frac{1}{T^{\mathtt{D}}} + \frac{1}{T_2^{\mathtt{SD}}} = \frac{1}{T^{\mathtt{D}}} + \bar{v}\,[A]\,\sigma_{\mathtt{SD}}^{A-A} + \sum \bar{v}\,[B]\,\sigma_{\mathtt{SD}}^{A-B} \tag{A.0.1}$$

where the rightmost term describes the relaxation due to collisions with buffer gas atoms that might be present, indices D, A and B stand for ”diffusion”, ”alkali” and ”buffer-gas”, correspondingly, and $\bar{v}[A]$ ($\bar{v}[B]$) is the mean relative alkali-alkali (alkali-buffer gas) thermal velocity. The role of the buffer gas is usually played by noble gases, which are used to slow down the alkali atoms so that they diffuse more slowly, a fact that increases the interaction time of the alkali atoms with the laser beams, which is a good thing in general. The reason for the use of noble gases is that the polarization of an alkali atom can survive millions of collisions with a noble gas atom without relaxing. However, the dephasing due to such collisions causes the linewidth of the transition to increase by factors on the order of 100 or more, depending primarily on the buffer gas density and species and secondarily on temperature. In high alkali densities, *radiation trapping* (the spontaneous emission and reabsorption of photons by the alkali atoms) can become a problem leading to fast spin relaxation. In these

Alkali metal	$\sigma^{\mathtt{SD}}_{\mathtt{self}}(\mathtt{cm}^2)$	$\sigma^{\mathtt{SD}}_{\mathtt{He}}(\mathtt{cm}^2)$	$\sigma^{\mathtt{SD}}_{\mathtt{Ne}}(\mathtt{cm}^2)$	$\sigma^{\mathtt{SD}}_{\mathtt{N}_2}(\mathtt{cm}^2)$
K	1×10^{-18}	8×10^{-25}	1×10^{-23}	
Rb	9×10^{-18}	9×10^{-24}		1×10^{-22}
Cs	2×10^{-16}	3×10^{-23}		6×10^{-22}

Table A.1: Common alkali-metal spin-destruction cross sections

cases a small amount of Nitrogen (a few tens of Torr) is used to *quench* the radiation, providing a non-radiative decay path. The most frequently used spin-destruction cross sections for$A$-B as well as A-A collisions are given in table A.1 (see [1] and references therein).

In the rest of this work and considering that it is a theoretical one, diffusion will be ignored, since it is mainly an experimental complication. This does not imply however that the effects of diffusion are negligible.

In Figure A.1, the rate $\frac{1}{T_2}$ is plotted for Rb atoms versus temperature and atom number density.

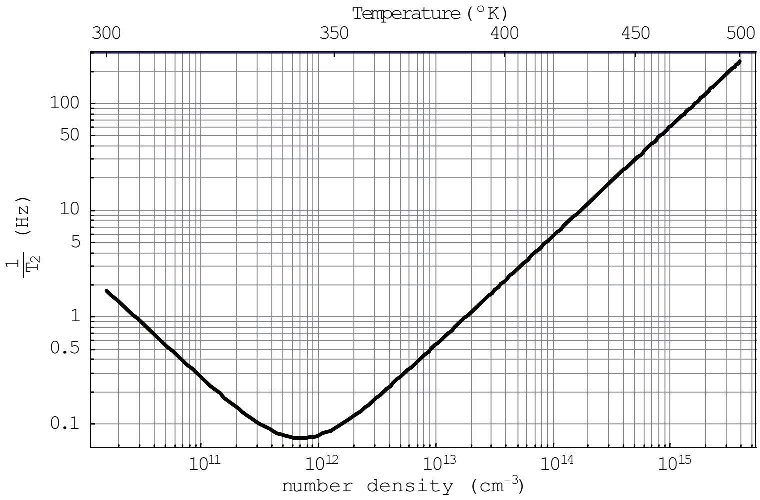

Figure A.1: $1/T_2$ for Rb versus atom number density

Appendix B

Rotations

When studying the pump-probe magnetometer or its EIT-enhanced version in the density matrix approach (via the Liouville equation), they both present the following difficulty: they involve fields in all 3 axes. There is the magnetic field along $\hat{\boldsymbol{y}}$, the pump field along $\hat{\boldsymbol{z}}$ and the probe (and the drive, in the EIT case) along $\hat{\boldsymbol{x}}$. To solve the Liouville equation though, one has to express all fields and relaxations along *one* quantization axis. So if some interaction matrix is expressed along a different quantization axis it will have to be rotated and be expressed along the quantization axis in use.

Specifically, in the toy models of Chapters 1 and 3, the pumping matrix is most easily defined along $\hat{\boldsymbol{z}}$ (its propagation direction) and the magnetic field Hamiltonian along $\hat{\boldsymbol{y}}$. Since we solve along $\hat{\boldsymbol{x}}$ (the propagation direction of the probe), these matrices have to be expressed along this axis. In the full level models of Chapter 4, rotation of the pumping matrix is quite difficult. In these cases we rotate and express every other matrix along the propagation direction of the pump beam ($\hat{\boldsymbol{z}}$), solve the Liouville equations and, then, rotate the resulting density matrix back along $\hat{\boldsymbol{x}}$. Here we will define and explain the various types of rotations.

B.1 $J = 1/2$ systems

B.1.1 Rotations of state operators

Consider the wavefunction of a spin-$\frac{1}{2}$ particle in a *pure state*[1] and let $\hat{\boldsymbol{z}}$ be the quantization axis [2]:

$$|\psi\rangle_{(z)} = c_{\downarrow}|-1/2\rangle_{(z)} + c_{\uparrow}|+1/2\rangle_{(z)} \equiv \begin{pmatrix} c_{\downarrow} \\ c_{\uparrow} \end{pmatrix} \tag{B.1.1}$$

The state of the system is equally well described by the density matrix corresponding to this wavefunction:

$$\rho_z = \langle\psi| \begin{pmatrix} |-1/2\rangle\langle -1/2| & |-1/2\rangle\langle +1/2| \\ |+1/2\rangle\langle -1/2| & |+1/2\rangle\langle +1/2| \end{pmatrix} |\psi\rangle = \begin{pmatrix} \rho_{\downarrow\downarrow} & \rho_{\downarrow\uparrow} \\ \rho_{\uparrow\downarrow} & \rho_{\uparrow\uparrow} \end{pmatrix} \tag{B.1.2}$$

where $\rho_{\downarrow\downarrow} \equiv |c_{\downarrow}|^2$, $\rho_{\uparrow\uparrow} \equiv |c_{\uparrow}|^2$ and $\rho_{\downarrow\uparrow} \equiv (c_{\downarrow})^* c_{\uparrow} = \rho^*_{\uparrow\downarrow}$.

The question is how is this system described along different axes. To find out, we can either *rotate* our coordinate system (say clockwise) by the desired angle about some appropriate axis or we can rotate the wavefunction itself by the same amount as in the former case, but in the opposite direction (counterclockwise). The two possibilities are called *passive* and *active* rotations, respectively, and effectively correspond to the case where an object can be seen from various directions either by the observer going around it or by the object itself being rotated. The whole idea is based on the belief that the laws of physics are the same in all directions in space.

A piece of information which is easily obtained from the equations above is the polarizations along arbitrary axes, that is the difference in the probabilities of states

---

[1] a pure state of a system is a state comprised of a coherent superposition of the basis states of the system. An incoherent superposition of the basis states is termed a *mixed state*. Pure states can be described by wavefunctions, whereas mixed states can not.

[2] Coefficients of the $|-1/2\rangle$ and $|+1/2\rangle$ states will be subscripted respectively with $\odot$ and $\otimes$ in the $\hat{\boldsymbol{x}}$-axis, $\downarrow$ and $\uparrow$ in the $\hat{\boldsymbol{z}}$-axis and with $\leftarrow$ and $\rightarrow$ in the $\hat{\boldsymbol{y}}$-axis

$|-1/2\rangle$ and $|+1/2\rangle$[3]. All one has to do is to evaluate the expectation values of the Pauli matrices:

$$\sigma_x = \begin{pmatrix} 0 & 1 \\ 1 & 0 \end{pmatrix}, \quad \sigma_y = \begin{pmatrix} 0 & -i \\ i & 0 \end{pmatrix} \quad \texttt{and} \quad \sigma_z = \begin{pmatrix} 1 & 0 \\ 0 & -1 \end{pmatrix} \tag{B.1.3}$$

We thus have[4]:

$$\begin{aligned} P_x \equiv \langle \sigma_x \rangle &= \langle \psi | \sigma_x | \psi \rangle = Tr(\rho_z \cdot \sigma_x) = 2\ \Re(\rho_{\uparrow\downarrow}) \\ P_y \equiv \langle \sigma_y \rangle &= \langle \psi | \sigma_y | \psi \rangle = Tr(\rho_z \cdot \sigma_y) = 2\ \Im(\rho_{\uparrow\downarrow}) \\ P_z \equiv \langle \sigma_z \rangle &= \langle \psi | \sigma_z | \psi \rangle = Tr(\rho_z \cdot \sigma_z) = \rho_{\downarrow\downarrow}\ -\ \rho_{\uparrow\uparrow} \end{aligned} \tag{B.1.4}$$

More generally, for an arbitrary direction defined by a unit vector $\hat{\boldsymbol{u}}$ with azimuthal angle θ and polar angle ϕ, $\hat{\boldsymbol{u}} = (\sin\theta\cos\phi,\ \sin\theta\sin\phi,\ \cos\theta)$, the corresponding Pauli matrix will be:

$$\sigma_u = \hat{\boldsymbol{u}} \cdot \boldsymbol{\sigma} = \begin{pmatrix} \cos\theta & e^{-i\phi}\sin\theta \\ e^{i\phi}\sin\theta & -\cos\theta \end{pmatrix} \tag{B.1.5}$$

where $\boldsymbol{\sigma} = (\sigma_x, \sigma_y, \sigma_z)$ and the polarization along $\hat{\boldsymbol{u}}$:

$$P_u \equiv \langle \sigma_u \rangle = Tr(\rho_z \cdot \sigma_u) = \sin\theta \left(e^{i\phi}\rho_{\downarrow\uparrow} + e^{-i\phi}\rho_{\uparrow\downarrow} \right) + \cos\theta \left(\rho_{\downarrow\downarrow} - \rho_{\uparrow\uparrow} \right) \tag{B.1.6}$$

However, polarizations alone do not provide a complete description of the system along an axis. What does is a rotation of the state vector or density matrix so that it coincides with the axis of interest. Since the Pauli matrices are the generators of rotations for spin-$\frac{1}{2}$ systems, a rotation through angle δ about an axis defined by the unit vector $\hat{\boldsymbol{u}}$ will be performed by the operator:

---

[3] Obviously, for a spin-1/2 particle, the polarization along some axis is two times the expectation value of the spin along that axis

[4] An important note about ρ: the importance of the density matrix formulation stems from the fact that whereas a pure state can always be described by a density matrix, a density matrix is a more general object also describing *mixed states* which can not be represented by a wavefunction. Thus, the expression $\langle A \rangle = Tr(\rho \cdot A)$ is true, even when $\langle A \rangle = \langle \psi | A | \psi \rangle$ lacks meaning.

$$R_u(\delta) = e^{-\frac{i}{2}\delta \hat{\boldsymbol{u}}\cdot\boldsymbol{\sigma}} \tag{B.1.7}$$

which has the well known property:

$$R_u(-\delta) = R_u^{-1}(\delta) = R_u^{\dagger}(\delta) \tag{B.1.8}$$

Thus the rotated wavefunction will be:

$$|\psi\,'\rangle = R_u(\delta)|\psi\rangle \tag{B.1.9}$$

and the rotated density matrix:

$$\rho\,' = |\psi\,'\rangle\langle\psi\,'| = R_u(\delta)\cdot\rho\cdot R_u^{\dagger}(\delta) \tag{B.1.10}$$

As an example we will see how the $\hat{\boldsymbol{z}}$-axis wavefunction (B.1.1) and density matrix (B.1.2) are expressed in $\hat{\boldsymbol{x}}$-axis. To rotate from $\hat{\boldsymbol{z}}$ to $\hat{\boldsymbol{x}}$ one has to perform a counter-clockwise rotation about $\hat{\boldsymbol{y}}$ through a $-\pi/2$ angle. Thus the $\hat{\boldsymbol{z}}$ basis vectors in terms of the $\hat{\boldsymbol{x}}$ basis vectors will be:

$$\begin{aligned} |-1/2\rangle_{z(x)} &= R_y(-\pi/2)|-1/2\rangle_{(z)} = \frac{1}{\sqrt{2}}\big(|-1/2\rangle_{(x)} - |+1/2\rangle_{(x)}\big) \\ |+1/2\rangle_{z(x)} &= R_y(-\pi/2)|+1/2\rangle_{(z)} = \frac{1}{\sqrt{2}}\big(|-1/2\rangle_{(x)} + |+1/2\rangle_{(x)}\big) \end{aligned} \tag{B.1.11}$$

and the rotated wavefunction along $\hat{\boldsymbol{x}}$:

$$|\psi\rangle_{(x)} = R_y(-\pi/2)|\psi\rangle_{(z)} \equiv c_{\odot}|-1/2\rangle_{(x)} + c_{\otimes}|+1/2\rangle_{(x)} \tag{B.1.12}$$

with $c_{\odot} = (c_{\uparrow} + c_{\downarrow})/\sqrt{2}$ and $c_{\otimes} = (c_{\uparrow} - c_{\downarrow})/\sqrt{2}$. Correspondingly, the rotated density matrix is given by:

$$\begin{aligned}\rho_x &= R_y(-\pi/2)\cdot\rho_z\cdot R_y^\dagger(-\pi/2) = \begin{pmatrix}\rho_{\odot\odot} & \rho_{\odot\otimes}\\ \rho_{\otimes\odot} & \rho_{\otimes\otimes}\end{pmatrix}\\ &= \frac{1}{2}\begin{pmatrix}\rho_{\uparrow\uparrow}+\rho_{\downarrow\downarrow}+2\,\Re(\rho_{\uparrow\downarrow}) & \rho_{\uparrow\uparrow}-\rho_{\downarrow\downarrow}-2\,\Im(\rho_{\uparrow\downarrow})\\ \rho_{\uparrow\uparrow}-\rho_{\downarrow\downarrow}+2\,\Im(\rho_{\uparrow\downarrow}) & \rho_{\uparrow\uparrow}+\rho_{\downarrow\downarrow}-2\,\Re(\rho_{\uparrow\downarrow})\end{pmatrix}\end{aligned} \tag{B.1.13}$$

from which we confirm that $P_x \equiv \rho_{\odot\odot} - \rho_{\otimes\otimes} = 2\,\Re\rho_{\uparrow\downarrow}$ [see eq.(B.1.4)].

B.1.2 Rotations of observables

Consider an observable quantity, A, of a spin-1/2 system. Let the observable be described by the operator $\hat{A}$ and the system by a density matrix ρ along some quantization axis. The expectation value of A will be:

$$A = \langle\hat{A}\rangle = Tr(\rho\hat{A}) \tag{B.1.14}$$

Since the expectation value of A must not be affected by a rotation of the coordinate system, if we rotate the density matrix about axis $\hat{\boldsymbol{u}}$ through an angle δ, so that ρ is transformed into $\rho\,' = R_u(\delta)\rho R_u^\dagger(\delta)$, then the operator $\hat{A}$ will also have to be transformed to some $\hat{A}'$, in a way that $\langle\hat{A}'\rangle = \langle\hat{A}\rangle$. This gives:

$$\langle\hat{A}'\rangle = Tr(\rho\,'\hat{A}') = Tr(R_u(\delta)\rho R_u^\dagger(\delta)\hat{A}') = Tr(\rho R_u^\dagger(\delta)\hat{A}' R_u(\delta)) = \langle\hat{A}\rangle$$

and thus, in conjunction with eq.(B.1.14):

$$\hat{A}' = R_u(\delta)\cdot\hat{A}\cdot R_u^\dagger(\delta) \tag{B.1.15}$$

B.1.3 Rotations of incoherent matrices

In both the EIT and TLA pump-probe magnetometers described in this work, the pumping beam acting along $\hat{\boldsymbol{z}}$-axis is described by an incoherent pumping matrix, $\mathcal{R}_{\mathrm{P}}(\rho)$, written down with respect to this particular quantization axis. Since we always work along $\hat{\boldsymbol{x}}$-axis, which is the propagation direction of the probe beam, this matrix has to be rotated about $\hat{\boldsymbol{y}}$ through $-\pi/2$. However, such matrices which describe incoherent procedures can not be rotated through a simple transformation of the form $[\mathcal{R}_{\mathrm{P}}(\rho)]_{(x)} = R_y(-\pi/2)\cdot[\mathcal{R}_{\mathrm{P}}(\rho)]_{(z)}\cdot R_y^{\dagger}(-\pi/2)$. In the following we give the procedure for rotating the TLA magnetometer pumping matrix from $\hat{\boldsymbol{z}}$-axis to $\hat{\boldsymbol{x}}$-axis (the EIT case is identical with just two extra rows and columns).

The density matrix along $\hat{\boldsymbol{z}}$-axis is:

$$\varrho = \begin{pmatrix} \varrho_{\bar{g}\bar{g}} & \varrho_{\bar{g}e} & \varrho_{\bar{g}g} & \varrho_{\bar{g}\bar{e}} \\ \varrho_{\bar{g}e}^{*} & \varrho_{ee} & \varrho_{ge}^{*} & \varrho_{\bar{e}e}^{*} \\ \varrho_{\bar{g}g}^{*} & \varrho_{ge} & \varrho_{gg} & \varrho_{g\bar{e}} \\ \varrho_{\bar{g}\bar{e}}^{*} & \varrho_{\bar{e}e} & \varrho_{g\bar{e}}^{*} & \varrho_{\bar{e}\bar{e}} \end{pmatrix} \tag{B.1.16}$$

and along $\hat{\boldsymbol{x}}$-axis:

$$\rho = \begin{pmatrix} \rho_{\bar{g}\bar{g}} & \rho_{\bar{g}e} & \rho_{\bar{g}g} & \rho_{\bar{g}\bar{e}} \\ \rho_{\bar{g}e}^{*} & \rho_{ee} & \rho_{ge}^{*} & \rho_{\bar{e}e}^{*} \\ \rho_{\bar{g}g}^{*} & \rho_{ge} & \rho_{gg} & \rho_{g\bar{e}} \\ \rho_{\bar{g}\bar{e}}^{*} & \rho_{\bar{e}e} & \rho_{g\bar{e}}^{*} & \rho_{\bar{e}\bar{e}} \end{pmatrix} = R_y(-\pi/2)\cdot\varrho\cdot R_y^{\dagger}(-\pi/2) \tag{B.1.17}$$

where we use ρ and ϱ to denote $\hat{\boldsymbol{x}}$ and $\hat{\boldsymbol{z}}$ density matrix elements, respectively[5]. In detail, the expressions of ρ in terms of ϱ and vice versa are given by:

$$\rho = \frac{1}{2}\begin{pmatrix} \varrho_{\bar{g}g}^{*} + \varrho_{\bar{g}g} + \varrho_{\bar{g}\bar{g}} + \varrho_{gg} & \varrho_{\bar{g}e} - \varrho_{\bar{g}\bar{e}} - \varrho_{g\bar{e}} + \varrho_{ge} & -\varrho_{\bar{g}g}^{*} + \varrho_{\bar{g}g} - \varrho_{\bar{g}\bar{g}} + \varrho_{gg} & \varrho_{\bar{g}e} + \varrho_{\bar{g}\bar{e}} + \varrho_{g\bar{e}} + \varrho_{ge} \\ \varrho_{\bar{g}e}^{*} - \varrho_{\bar{g}\bar{e}}^{*} - \varrho_{g\bar{e}}^{*} + \varrho_{ge}^{*} & -\varrho_{\bar{e}e}^{*} - \varrho_{\bar{e}e} + \varrho_{\bar{e}\bar{e}} + \varrho_{ee} & -\varrho_{\bar{g}e}^{*} + \varrho_{\bar{g}\bar{e}}^{*} - \varrho_{g\bar{e}}^{*} + \varrho_{ge}^{*} & \varrho_{\bar{e}e}^{*} - \varrho_{\bar{e}e} - \varrho_{\bar{e}\bar{e}} + \varrho_{ee} \\ \varrho_{\bar{g}g}^{*} - \varrho_{\bar{g}g} - \varrho_{\bar{g}\bar{g}} + \varrho_{gg} & -\varrho_{\bar{g}e} + \varrho_{\bar{g}\bar{e}} - \varrho_{g\bar{e}} + \varrho_{ge} & -\varrho_{\bar{g}g}^{*} - \varrho_{\bar{g}g} + \varrho_{\bar{g}\bar{g}} + \varrho_{gg} & -\varrho_{\bar{g}e} - \varrho_{\bar{g}\bar{e}} + \varrho_{g\bar{e}} + \varrho_{ge} \\ \varrho_{\bar{g}e}^{*} + \varrho_{\bar{g}\bar{e}}^{*} + \varrho_{g\bar{e}}^{*} + \varrho_{ge}^{*} & -\varrho_{\bar{e}e}^{*} + \varrho_{\bar{e}e} - \varrho_{\bar{e}\bar{e}} + \varrho_{ee} & -\varrho_{\bar{g}e}^{*} - \varrho_{\bar{g}\bar{e}}^{*} + \varrho_{g\bar{e}}^{*} + \varrho_{ge}^{*} & \varrho_{\bar{e}e}^{*} + \varrho_{\bar{e}e} + \varrho_{\bar{e}\bar{e}} + \varrho_{ee} \end{pmatrix} \tag{B.1.18}$$

---

[5] notation has always been one of the greatest obstacles in the study of mathematics and physics

$$\varrho = \frac{1}{2}\begin{pmatrix} -\rho^*_{\bar{g}g} - \rho_{\bar{g}g} + \rho_{\bar{g}\bar{g}} + \rho_{gg} & \rho_{\bar{g}e} + \rho_{\bar{g}\bar{e}} - \rho_{g\bar{e}} - \rho_{ge} & -\rho^*_{\bar{g}g} + \rho_{\bar{g}g} + \rho_{\bar{g}\bar{g}} - \rho_{gg} & -\rho_{\bar{g}e} + \rho_{\bar{g}\bar{e}} - \rho_{g\bar{e}} + \rho_{ge} \\ \rho^*_{\bar{g}e} + \rho^*_{\bar{g}\bar{e}} - \rho^*_{g\bar{e}} - \rho^*_{ge} & \rho^*_{\bar{e}e} + \rho_{\bar{e}e} + \rho_{\bar{e}\bar{e}} + \rho_{ee} & \rho^*_{\bar{g}e} + \rho^*_{\bar{g}\bar{e}} + \rho^*_{g\bar{e}} + \rho^*_{ge} & \rho^*_{\bar{e}e} - \rho_{\bar{e}e} + \rho_{\bar{e}\bar{e}} - \rho_{ee} \\ \rho^*_{\bar{g}g} - \rho_{\bar{g}g} + \rho_{\bar{g}\bar{g}} - \rho_{gg} & \rho_{\bar{g}e} + \rho_{\bar{g}\bar{e}} + \rho_{g\bar{e}} + \rho_{ge} & \rho^*_{\bar{g}g} + \rho_{\bar{g}g} + \rho_{\bar{g}\bar{g}} + \rho_{gg} & -\rho_{\bar{g}e} + \rho_{\bar{g}\bar{e}} + \rho_{g\bar{e}} - \rho_{ge} \\ -\rho^*_{\bar{g}e} + \rho^*_{\bar{g}\bar{e}} - \rho^*_{g\bar{e}} + \rho^*_{ge} & -\rho^*_{\bar{e}e} + \rho_{\bar{e}e} + \rho_{\bar{e}\bar{e}} - \rho_{ee} & -\rho^*_{\bar{g}e} + \rho^*_{\bar{g}\bar{e}} + \rho^*_{g\bar{e}} - \rho^*_{ge} & -\rho^*_{\bar{e}e} - \rho_{\bar{e}e} + \rho_{\bar{e}\bar{e}} + \rho_{ee} \end{pmatrix} \tag{B.1.19}$$

Now the rate of change of ϱ due to the pumping rate will be described by:

$$\frac{d\varrho}{dt} \propto [\mathcal{R}_{\mathtt{P}}(\rho)]_{(z)} = \frac{R_{\mathtt{ex}}}{2}\begin{pmatrix} -2\varrho_{\bar{g}\bar{g}} & -\varrho_{\bar{g}e} & -\varrho_{\bar{g}g} & -\varrho_{\bar{g}\bar{e}} \\ -\varrho^*_{\bar{g}e} & 2\varrho_{\bar{g}\bar{g}} & 0 & 0 \\ -\varrho^*_{\bar{g}g} & 0 & 0 & 0 \\ -\varrho^*_{\bar{g}\bar{e}} & 0 & 0 & 0 \end{pmatrix} \tag{B.1.20}$$

Expressing ϱ in terms of ρ in both the left and right hand sides of equation (B.1.20) and solving for the ρ's, we find the expression of the pumping matrix along $\hat{\boldsymbol{x}}$-axis:

$$\frac{d\rho}{dt} \propto [\mathcal{R}_{\mathtt{P}}(\rho)]_{(x)} = \tag{B.1.21}$$

$$= \frac{R_{\mathtt{ex}}}{4}\begin{pmatrix} \rho^*_{\bar{g}g} + \rho_{\bar{g}g} - 2\rho_{\bar{g}\bar{g}} & \rho_{ge} - \rho_{\bar{g}e} & -2\rho_{\bar{g}g} + \rho_{\bar{g}\bar{g}} + \rho_{gg} & \rho_{g\bar{e}} - \rho_{\bar{g}\bar{e}} \\ \rho^*_{ge} - \rho^*_{\bar{g}e} & -\rho^*_{\bar{g}g} - \rho_{\bar{g}g} + \rho_{\bar{g}\bar{g}} + \rho_{gg} & \rho^*_{\bar{g}e} - \rho^*_{ge} & -\rho^*_{\bar{g}g} - \rho_{\bar{g}g} + \rho_{\bar{g}\bar{g}} + \rho_{gg} \\ -2\rho^*_{\bar{g}g} + \rho_{\bar{g}\bar{g}} + \rho_{gg} & \rho_{\bar{g}e} - \rho_{ge} & \rho^*_{\bar{g}g} + \rho_{\bar{g}g} - 2\rho_{gg} & \rho_{\bar{g}\bar{e}} - \rho_{g\bar{e}} \\ \rho^*_{g\bar{e}} - \rho^*_{\bar{g}\bar{e}} & -\rho^*_{\bar{g}g} - \rho_{\bar{g}g} + \rho_{\bar{g}\bar{g}} + \rho_{gg} & \rho^*_{\bar{g}\bar{e}} - \rho^*_{g\bar{e}} & -\rho^*_{\bar{g}g} - \rho_{\bar{g}g} + \rho_{\bar{g}\bar{g}} + \rho_{gg} \end{pmatrix}$$

Closing this discussion, we note that the total relaxation matrix, $\mathcal{R}(\rho)$, in the Liouville equation (1.2.32) for the TLA or the EIT magnetometer scheme also includes the natural decay and $\frac{1}{T_2}$ relaxations, $\mathcal{R}_{\mathtt{N}}(\rho)$, that is:

$$\mathcal{R}(\rho) = \mathcal{R}_{\mathtt{N}}(\rho) + \mathcal{R}_{\mathtt{P}}(\rho) \tag{B.1.22}$$

where:

$$\mathcal{R}_{\mathtt{N}}(\rho) = \begin{pmatrix} \frac{\Gamma}{2}(\rho_{ee}+\rho_{\bar{e}\bar{e}}) + \frac{1}{T_2}\left(\frac{1}{2}-\rho_{\bar{g}\bar{g}}\right) & -\frac{\Gamma}{2}\rho_{\bar{g}e} & -\frac{1}{T_2}\rho_{\bar{g}g} & -\frac{\Gamma}{2}\rho_{\bar{g}\bar{e}} \\ -\frac{\Gamma}{2}\rho^*_{\bar{g}e} & -\Gamma\rho_{ee} & -\frac{\Gamma}{2}\rho^*_{ge} & -\Gamma\rho^*_{\bar{e}e} \\ -\frac{1}{T_2}\rho^*_{\bar{g}g} & -\frac{\Gamma}{2}\rho_{ge} & \frac{\Gamma}{2}(\rho_{ee}+\rho_{\bar{e}\bar{e}}) + \frac{1}{T_2}\left(\frac{1}{2}-\rho_{gg}\right) & -\frac{\Gamma}{2}\rho_{g\bar{e}} \\ -\frac{\Gamma}{2}\rho^*_{\bar{g}\bar{e}} & -\Gamma\rho_{\bar{e}e} & -\frac{\Gamma}{2}\rho^*_{g\bar{e}} & -\Gamma\rho_{\bar{e}\bar{e}} \end{pmatrix} \tag{B.1.23}$$

For the sake of completeness we write below the corresponding quantities for the EIT case. The relaxation matrix is defined as:

$$\mathcal{R}(\rho) = \mathcal{R}_{\mathtt{N}}(\rho) + \mathcal{R}_{\mathtt{P}}(\rho) \tag{B.1.24}$$

where

$$\mathcal{R}_{\mathtt{N}}(\rho) = \begin{pmatrix} \left[\mathcal{R}_{\mathtt{N}[\Lambda_1]}\right] & \left[\mathcal{R}_{\mathtt{N}[\Lambda_{12}]}\right] \\ \left[\mathcal{R}^{\dagger}_{\mathtt{N}[\Lambda_{12}]}\right] & \left[\mathcal{R}_{\mathtt{N}[\Lambda_2]}\right] \end{pmatrix} \tag{B.1.25}$$

with:

$$\mathcal{R}_{\mathtt{N}[\Lambda_1]} = \begin{pmatrix} \frac{\Gamma}{4}(\rho_{ee}+\rho_{\bar{e}\bar{e}}) + \frac{1}{T_2}\left(\frac{1}{4}-\rho_{\bar{g}\bar{g}}\right) & -\frac{\Gamma}{2}\rho_{\bar{g}e} & -\gamma_{gc}\rho_{\bar{g}\bar{c}} \\ -\frac{\Gamma}{2}\rho^*_{\bar{g}e} & -\Gamma\rho_{ee} & -\frac{\Gamma}{2}\rho^*_{\bar{c}e} \\ -\gamma_{gc}\rho^*_{\bar{g}\bar{c}} & -\frac{\Gamma}{2}\rho_{\bar{c}e} & \frac{\Gamma}{4}(\rho_{ee}+\rho_{\bar{e}\bar{e}}) + \frac{1}{T_2}\left(\frac{1}{4}-\rho_{\bar{c}\bar{c}}\right) \end{pmatrix} \tag{B.1.26}$$

$$\mathcal{R}_{\mathtt{N}[\Lambda_2]} = \begin{pmatrix} \frac{\Gamma}{4}(\rho_{ee}+\rho_{\bar{e}\bar{e}}) + \frac{1}{T_2}\left(\frac{1}{4}-\rho_{gg}\right) & -\frac{\Gamma}{2}\rho_{g\bar{e}} & -\gamma_{gc}\rho_{gc} \\ -\frac{\Gamma}{2}\rho^*_{g\bar{e}} & -\Gamma\rho_{ee} & -\frac{\Gamma}{2}\rho^*_{c\bar{e}} \\ -\gamma_{gc}\rho^*_{gc} & -\frac{\Gamma}{2}\rho_{c\bar{e}} & \frac{\Gamma}{4}(\rho_{ee}+\rho_{\bar{e}\bar{e}}) + \frac{1}{T_2}\left(\frac{1}{4}-\rho_{cc}\right) \end{pmatrix} \tag{B.1.27}$$

$$\mathcal{R}_{\mathtt{N}[\Lambda_{12}]} = \begin{pmatrix} -\frac{1}{T_2}\rho_{\bar{g}g} & -\frac{\Gamma}{2}\rho_{\bar{g}\bar{e}} & -\gamma_{gc}\rho_{\bar{g}c} \\ -\frac{\Gamma}{2}\rho^*_{ge} & -\Gamma\rho^*_{\bar{e}e} & -\frac{\Gamma}{2}\rho^*_{ce} \\ -\gamma_{gc}\rho^*_{g\bar{c}} & -\frac{\Gamma}{2}\rho_{\bar{c}\bar{e}} & -\frac{1}{T_2}\rho_{\bar{c}c} \end{pmatrix} \tag{B.1.28}$$

and

$$\mathcal{R}_{\mathtt{P}}(\rho) = -R \begin{pmatrix} \left[\mathcal{R}_{\mathtt{P}[\Lambda_1]}\right] & \left[\mathcal{R}_{\mathtt{P}[\Lambda_{12}]}\right] \\ \left[\mathcal{R}^{\dagger}_{\mathtt{P}[\Lambda_{12}]}\right] & \left[\mathcal{R}_{\mathtt{P}[\Lambda_2]}\right] \end{pmatrix} \tag{B.1.29}$$

where $R = \frac{R_{\mathrm{ex}}}{4}$ and:

$$\mathcal{R}_{\mathtt{P}[\Lambda_1]} = \begin{pmatrix} 2\rho_{\bar{g}\bar{g}} - \rho_{\bar{g}g} - \rho^*_{\bar{g}g} & \rho_{\bar{g}e} - \rho_{ge} & \rho_{\bar{g}\bar{c}} - \rho_{g\bar{c}} \\ \rho^*_{\bar{g}e} - \rho^*_{ge} & \rho_{gg} + \rho_{\bar{g}\bar{g}} - \rho_{\bar{g}g} - \rho^*_{\bar{g}g} & 0 \\ \rho^*_{\bar{g}\bar{c}} - \rho^*_{g\bar{c}} & 0 & 0 \end{pmatrix} \tag{B.1.30}$$

$$\mathcal{R}_{\mathtt{P}[\Lambda_2]} = \begin{pmatrix} 2\rho_{gg} - \rho_{\bar{g}g} - \rho^*_{\bar{g}g} & \rho_{g\bar{e}} - \rho_{\bar{g}\bar{e}} & \rho_{gc} - \rho_{\bar{g}c} \\ \rho^*_{g\bar{e}} - \rho^*_{\bar{g}\bar{e}} & \rho_{gg} + \rho_{\bar{g}\bar{g}} - \rho_{\bar{g}g} - \rho^*_{\bar{g}g} & 0 \\ \rho^*_{gc} - \rho^*_{\bar{g}c} & 0 & 0 \end{pmatrix} \tag{B.1.31}$$

$$\mathcal{R}_{\mathtt{P}[\Lambda_{12}]} = \begin{pmatrix} 2\rho_{\bar{g}g} - \rho_{\bar{g}\bar{g}} - \rho_{gg} & \rho_{\bar{g}\bar{e}} - \rho_{g\bar{e}} & \rho_{\bar{g}c} - \rho_{gc} \\ \rho^*_{\bar{g}\bar{e}} - \rho^*_{g\bar{e}} & \rho_{gg} + \rho_{\bar{g}\bar{g}} - \rho_{\bar{g}g} - \rho^*_{\bar{g}g} & 0 \\ \rho^*_{\bar{g}c} - \rho^*_{gc} & 0 & 0 \end{pmatrix} \tag{B.1.32}$$

B.2 $J \geq 1/2$ systems

An arbitrary rotation about an arbitrary axis of the density matrix (or of an observable) of a system with total angular momentum J can be performed either by direct rotation about the given axis, or, equivalently, by three successive rotations:

- one rotation about the quantization axis (let $\hat{\boldsymbol{z}}$ be it) through an angle α
- one rotation about an axis perpendicular to the quantization axis (if the system is quantized along $\hat{\boldsymbol{z}}$, then $\hat{\boldsymbol{y}}$ is customarily used as the second rotation axis) through an angle β
- one rotation about the quantization axis through an angle γ

The angles α, β and γ are called *Euler angles* and are determined by the orientation of the axis about which we actually want to rotate and by the desired rotation angle.

If the density matrix of the system is put in the form:

$$\rho = \begin{pmatrix} \rho_{-j,-j} & \rho_{-j,-j+1} & \cdots & \rho_{-j,j} \\ \rho_{-j+1,-j} & \rho_{-j+1,-j+1} & \cdots & \rho_{-j+1,j} \\ \vdots & \vdots & \ddots & \vdots \\ \rho_{j,-j} & \rho_{j,-j+1} & \cdots & \rho_{j,j} \end{pmatrix} \tag{B.2.1}$$

then the rotation matrix about $\hat{\boldsymbol{z}}$-axis is given by:

$$U_z(\theta) = \begin{pmatrix} e^{i(-j)\theta} & 0 & \cdots & 0 \\ 0 & e^{i(-j+1)\theta} & \cdots & 0 \\ \vdots & \vdots & \ddots & \vdots \\ 0 & 0 & \cdots & e^{ij\theta} \end{pmatrix} \tag{B.2.2}$$

while the rotation matrix about $\hat{\boldsymbol{y}}$-axis is more complicated and its elements are given by [15]:

$$U_y(\theta) = \sqrt{(j-m_f)!\,(j+m_f)!\,(j-m_i)!\,(j+m_i)!}\,\times \tag{B.2.3}$$

$$\tag{B.2.4}$$

$$\sum_{k=\max\left(0,m_f-m_i\right)}^{\min\left(j+m_f,j-m_i\right)} \frac{(-1)^k \cos^{2(j-k)+m_f-m_i}\left(\frac{\theta}{2}\right) \sin^{2k-m_f+m_i}\left(\frac{\theta}{2}\right)}{k!\,(j-k+m_f)!\,(j-k-m_i)!\,(k-m_f+m_i)!} \tag{B.2.5}$$

with $m_i,\ m_f = -j, -j+1, ..., j-1, j$. Thus, a rotation of ρ through the Euler angles α, β, γ takes the form:

$$\rho\,' = U_z(\gamma)\cdot U_y(\beta)\cdot U_z(\alpha)\cdot \rho \cdot U_z^\dagger(\alpha)\cdot U_y^\dagger(\beta)\cdot U_z^\dagger(\gamma) \tag{B.2.6}$$

Of course one is not obliged to quantize a system along $\hat{\boldsymbol{z}}$. If a different direction is used for the quantization, the following table gives the second rotation axis:

Quantization axis	Second rotation about...
$\hat{\boldsymbol{x}}$	$\hat{\boldsymbol{z}}$
$\hat{\boldsymbol{y}}$	$\hat{\boldsymbol{x}}$
$\hat{\boldsymbol{z}}$	$\hat{\boldsymbol{y}}$

In the text we will be using various axes as quantization axes. If rotations are necessary we will be referring to rotations about the quantization axis as *z-type rotations* [rotation matrix given by eq.(B.2.2)] and to rotations about the corresponding perpendicular axis as *y-type rotations* [rotation matrix given by eq.(B.2.3)].

Appendix C

Density matrix vs Bloch approach in the P-P magnetometer

To establish the equivalence between the density matrix approach and the Bloch equations, we set $\Omega = 0$ and replace the probe beam effect by the incoherent probe pumping matrix [1]:

$$\mathcal{R}_{\texttt{probe}}(\rho) = \begin{pmatrix} -R_{\texttt{probe}}\rho_{\bar{g}\bar{g}} & -\frac{R_{\texttt{probe}}}{2}\rho_{\bar{g}e} & -R_{\texttt{probe}}\rho_{\bar{g}g} & -\frac{R_{\texttt{probe}}}{2}\rho_{\bar{g}\bar{e}} \\ -\frac{R_{\texttt{probe}}}{2}\rho^*_{\bar{g}e} & R_{\texttt{probe}}\rho_{\bar{g}\bar{g}} & -\frac{R_{\texttt{probe}}}{2}\rho^*_{ge} & 0 \\ -R_{\texttt{probe}}\rho^*_{\bar{g}g} & -\frac{R_{\texttt{probe}}}{2}\rho_{ge} & -R_{\texttt{probe}}\rho_{gg} & -\frac{R_{\texttt{probe}}}{2}\rho_{g\bar{e}} \\ -\frac{R_{\texttt{probe}}}{2}\rho^*_{\bar{g}\bar{e}} & 0 & -\frac{R_{\texttt{probe}}}{2}\rho^*_{g\bar{e}} & R_{\texttt{probe}}\rho_{gg} \end{pmatrix} \tag{C.0.1}$$

We now eliminate the excited states from the Liouville equations, to arrive at the equations for $\rho_{\bar{g}\bar{g}}$, ρ_{gg} and $\rho_{\bar{g}g}$. This is done by solving for all elements involving states $|e\rangle$ and $|\bar{e}\rangle$ and substituting the solutions in the rest of the equations. We thus obtain:

---

[1] the reason for this manoeuvre is that the Bloch equations do not deal with coherent effects

$$
\begin{aligned}
\frac{d\rho_{\bar{g}\bar{g}}}{dt} &= \frac{1}{2\,T_2} - \left(\frac{R_{\texttt{ex}}}{2} + R_{\texttt{probe}} + \frac{1}{T_2}\right)\rho_{\bar{g}\bar{g}} + \frac{R_{\texttt{ex}} + 2\,\Omega_L}{4}(\rho_{\bar{g}g} + \rho^*_{\bar{g}g}) \\
\frac{d\rho_{gg}}{dt} &= \frac{1}{2\,T_2} - \left(\frac{R_{\texttt{ex}}}{2} + R_{\texttt{probe}} + \frac{1}{T_2}\right)\rho_{gg} + \frac{R_{\texttt{ex}} - 2\,\Omega_L}{4}(\rho_{\bar{g}g} + \rho^*_{\bar{g}g}) \qquad \text{(C.0.2)} \\
\frac{d\rho_{\bar{g}g}}{dt} &= \frac{R_{\texttt{ex}}}{4} - \left(\frac{R_{\texttt{ex}}}{2} + R_{\texttt{probe}} + \frac{1}{T_2}\right)\rho_{\bar{g}g} + \frac{\Omega_L}{2}(\rho_{gg} - \rho_{\bar{g}\bar{g}})
\end{aligned}
$$

We now use the correspondence between density matrix elements and polarizations, which is explained in Appendix B:

$$
\begin{aligned}
P_x &= \rho_{gg} - \rho_{\bar{g}\bar{g}} \\
P_y &= 2\,\Im(\rho_{\bar{g}g}) \qquad \text{(C.0.3)} \\
P_z &= 2\,\Re(\rho_{\bar{g}g})
\end{aligned}
$$

which is derived from equation (B.1.4) with $\hat{\boldsymbol{x}}$ as the quantization axis. After some manipulation of equations (C.0.2), we get:

$$
\begin{aligned}
\frac{dP_x}{dt} &= -\left(\frac{R_{\texttt{ex}}}{2} + R_{\texttt{probe}} + \frac{1}{T_2}\right)P_x - \Omega_L P_z \\
\frac{dP_y}{dt} &= -\left(\frac{R_{\texttt{ex}}}{2} + R_{\texttt{probe}} + \frac{1}{T_2}\right)P_y \qquad \text{(C.0.4)} \\
\frac{dP_z}{dt} &= \frac{R_{\texttt{ex}}}{2} - \left(\frac{R_{\texttt{ex}}}{2} + R_{\texttt{probe}} + \frac{1}{T_2}\right)P_z + \Omega_L P_x
\end{aligned}
$$

which coincide exactly with the Bloch equations (1.2.4), if we identify the optical pumping rate to equal half of the excitation rate, $R = R_{\texttt{ex}}/2$, which is true since we have supposed that the excited states decay to the ground states with the same rates. This completes the demonstration of the equivalence of the Bloch equation and density matrix approaches to the description of the TLA P-P magnetometer.

Appendix D

Complex refractive index vs density matrix

The index of refraction, n, of an isotropic absorptive medium is related to the complex linear susceptibility of the medium, χ, via the following relation:

$$n = n' + in'' = \sqrt{1+\chi} \tag{D.0.1}$$

where the real and imaginary parts of the refractive index are traditionally denoted by n' and n'', respectively. For a dilute gas it is $|\chi| \ll 1$ which allows the approximation $\sqrt{1+\chi} \simeq 1 + \frac{\chi}{2}$ and, since χ, like n, can be written in a complex form, $\chi = \chi' + i\chi''$, equation (D.0.1) leads to:

$$n' \simeq 1 + \frac{\chi'}{2} \tag{D.0.2}$$

$$n'' \simeq \frac{\chi''}{2} \tag{D.0.3}$$

If a transition $|g\rangle \leftrightarrow |e\rangle$ is probed by a weak monochromatic field, the complex polarization of atoms with number density n_d is given by:

$$P = n_d(\wp_{ge}\rho_{ge} + \wp_{ge}^{*}\rho_{ge}^{*}) \tag{D.0.4}$$

where $\wp_{ge}$ is the dipole matrix element for the $|g\rangle \leftrightarrow |e\rangle$ transition. The Fourier transform at the frequency of the field acting on the transition is given by:

$$P(\omega) = \epsilon_o \left[\chi'(\omega) + i\chi''(\omega)\right] E \tag{D.0.5}$$

which leads to:

$$\chi'(\omega) = \frac{n_d}{2\epsilon_o \hbar E}(\wp_{ge}\rho_{ge} + \wp^*_{ge}\rho^*_{ge}), \quad \chi''(\omega) = \frac{n_d}{2i\epsilon_o \hbar E}(\wp_{ge}\rho_{ge} - \wp^*_{ge}\rho^*_{ge}) \tag{D.0.6}$$

Assuming a real dipole matrix element and taking into account that the Rabi frequency of the laser is $\Omega = \frac{\wp_{ge}E}{\hbar}$, we see from equation (D.0.6) that the real and imaginary parts of the linear susceptibility are connected to the real and imaginary parts of the ρ_{ge} matrix elements, respectively, via:

$$\chi'(\omega) = \frac{n_d|\wp_{ge}|^2}{\epsilon_o \hbar\, \Omega}\, \Re(\rho_{ge}), \quad \chi''(\omega) = \frac{n_d|\wp_{ge}|^2}{\epsilon_o \hbar\, \Omega}\, \Im(\rho_{ge}) \tag{D.0.7}$$

Equation (D.0.7) shows that the dependence of ρ_{ge} on the detuning of the laser determines the frequency behavior of χ and, thus, of n, which in turn determines the dispersion and absorption profiles of the transition as explained in §1.2.5. The dipole matrix element $\wp_{ge}$ can also be substituted in eq.(D.0.7), by:

$$|\wp_{ge}|^2 = \frac{1}{2}\left(\frac{1}{2}+1\right)\, 4\pi\epsilon_o\, \frac{c^3}{\omega_{ge}^3}\, \hbar\Gamma \tag{D.0.8}$$

which, after substituting $\omega_{ge} = 2\pi c/\lambda_{ge}$, with λ_{ge} the vacuum transition wavelength of the $|g\rangle \leftrightarrow |e\rangle$ transition, and the normalized Rabi frequency $\tilde{\Omega} = \Omega/\Gamma$, leads to:

$$\chi'(\omega) = \frac{3n_d\lambda_{ge}^3}{8\pi^2\, \tilde{\Omega}}\, \Re(\rho_{ge}), \quad \chi''(\omega) = \frac{3n_d\lambda_{ge}^3}{8\pi^2\, \tilde{\Omega}}\, \Im(\rho_{ge}) \tag{D.0.9}$$

This very helpful relation is used in §1.2.5 for a rigorous derivation of the rotation angle and signal of the magnetometer.

Bibliography

[1] J.C. Allred, R.N. Lyman, T.W. Kornack, and M.V. Romalis, *High-sensitivity atomic magnetometer unaffected by spin-exchange relaxation*, Phys. Rev. Lett. **89** (2002), 130801.

[2] E. Arimondo, Progress in Optics **35** (1996), 257–354.

[3] D. Budker, D. Kimball, and D. DeMille, *Atomic physics*, Oxford University Press, Great Britain, 2004.

[4] M. Fleischhauer, A. Imamoglu, and J.P. Marangos, *Electromagnetically Induced Transparency: Optics in coherent media*, Rev. Mod. Phys. **77** (2005), 633.

[5] David Mc Gloin, *no se*, Ph.D. thesis, St. Andrews University, 1453.

[6] W. Happer and A.C. Tam, *Effect of rapid spin exchange on the magnetic-resonance spectrum of alkali vapors*, Phys. Rev. A **16** (1977), 1877–1891.

[7] W. Happer and H. Tang, *Spin-exchange shift and narrowing of magnetic resonance lines in optically pumped alkali vapors*, Phys. Rev. Lett. **31** (1973), 273–276.

[8] S. E. Harris, J. E. Field, and A. Imamoglu, *Nonlinear optical processes using electromagnetically induced transparency*, Phys. Rev. Lett. **64** (1990), 2813.

[9] S.E. Harris, *Lasers without inversion - interference of lifetime broadened resonances*, Phys. Rev. Lett. **62** (1989), 1033.

[10] O.A. Kocharovskaya and Y.I. Khanin, *Coherent amplification of an ultra-short pulse in a 3-level medium without population inversion*, JETP lett. **48** (1988), 630.

[11] I.K. Kominis, T.W. Kornack, J.C. Allred, and M.V. Romalis, *A subfemtotesla multichannel atomic magnetometer*, Nature **422** (2003), 596–599.

[12] F. Mandl, *Statistical physics*, John Wiley and Sons Ltd.

[13] J. Nenonen, J. Montonen, and T. Katila, *Thermal noise in biomagnetic measurements*, Rev. Sci. Instr. **67** (1996), 2397.

[14] I. I. Sobelman, *Atomic Spectra and Radiative Transitions*, second ed., Springer-Verlag, Berlin, 1992.

[15] William J. Thompson, *Angular Momentum*, John Wiley and Sons, 1994.

[16] T. Varpula and T. Poutanen, *Magnetic field fluctuations arising from thermal motion of electric charge in conductors*, J. Appl. Phys **55** (1984), 4015.

[17] D.J. Wineland, J.J. Bolinger, W.M. Itano, and D.J. Heinzen, *Squeezed atomic states and projection noise in spectroscopy*, Phys. Rev. A **50** (1994), 67.

[18] A.S. Zibrov, M.D. Lukin, L. Hollberg, D.E. Nikonov, M.O. Scully, and H.G. Robinson, *Experimental demonstration of enhanced index of refraction via quantum coherence in Rb*, Phys. Rev. Lett. **76** (1996), 3935–3938.